A Novel Current Source Converter-Based Ultra-High-Power Offshore Wind Energy Conversion System

by

Kaiwen Yang

Submitted in partial fulfillment of the requirements

for the degree of Master of Science in

Electrical and Computer Engineering

Lakehead University

Thunder Bay, Ontario

March 2025

Author's Declaration

I hereby declare that I am the sole author of this thesis. This is a true copy of the thesis, including any required final revisions, as accepted by my examiners.

Abstract

In medium voltage (MV) ultra-high-power (over 10 MW) offshore wind energy conversion systems (WECS), current source converter (CSC)-based series-connected configurations are a good candidate. However, existing CSC-based WECS use the bulky low-frequency transformer (LFT), have high rotor torque ripple or require the active rectifier, which entails higher costs, lower reliability and efficiency, and larger size and weight than the diode rectifier. To address these issues, this thesis proposes a novel CSC-based series-connected MV WECS, combining the six-phase generator connected to two diode rectifiers with two medium frequency transformers (MFTs)-based modular converters on the generator side and using the dual-bridge current source inverters (CSIs) on the grid side. The proposed WECS effectively mitigates rotor torque ripple caused by diode rectifiers and retains all the advantages of existing MFTs-based WECS. Additionally, the modular converter in the proposed WECS has voltage and current imbalance issues, so a corresponding control scheme is proposed to address these issues. Furthermore, online selective harmonic elimination (SHE) modulation is applied to the grid-side CSIs. This approach significantly reduces the memory requirements of the digital controller, thereby lowering costs while retaining all the advantages of conventional SHE techniques. The feasibility and effectiveness of the proposed WECS, its control scheme, and the online SHE modulation are validated through simulation results.

Acknowledgments

First and foremost, I would like to express my heartfelt gratitude to my supervisor, Dr. Qiang Wei, for his invaluable guidance, support, and encouragement throughout the course of my research. His expertise and mentorship have been instrumental in the successful completion of this work.

I am also deeply thankful to my course professors, Dr. Yushi Zhou for his insights into ASIC Design, Dr. Krishnamoorthy Natarajan for his guidance in Linear Algebra, and Dr. Xiaoping Liu for his teachings in Adaptive Control. Their knowledge and dedication have greatly enriched my learning experience and provided me with the foundation for my research.

I would like to extend my gratitude to my incredible team members: Zijian Wang, Javad, Milad, and Erfan. Their collaboration, support, and shared passion have made this journey both productive and enjoyable.

Also, I want to express my deepest appreciation to my girlfriend, Jiaqi Li, for her unwavering love, patience, and encouragement. Her belief in me has been a constant source of motivation and strength.

Last but not least, I would like to express my great thanks to my parents, who always supported me mentally and financially in pursuing knowledge and going broad and always stood by my side whenever I needed to.

To all of you, I am forever grateful for your contributions to this work and for being part of this meaningful journey.

Table of Contents

List of Figures

List of Tables

List of Symbols

Symbol	Meaning
v_{C1}, v_{C2}, …., v_{Cn}	input capacitor voltage of the modular converter
C_1, C_2, …., C_n	input series capacitor
i_{i1}, i_{i2}, …., i_{im}	cell input average current
V_{in}	input voltage of the modular converter
I_{con1}/I_{con2}	input current of the modular converter
v_{wind}	wind speed
ω_{ref}	generator speed reference
$i_{dc\text{-}gen}$	generator-side DC-link current reference
$i_{dc\text{-}grid}$	grid-side DC-link current reference
v_{cd}, v_{cq}	components of the *d*-axis and *q*-axis of the filter capacitor voltage
V_{gd}, V_{gq}	components of the *d*-axis and *q*-axis of grid-side voltage
$Q_{g\text{-}ref}$	grid reactive power reference
$i_{dc\text{-}ref}$	DC-link current reference
$i_{wq\text{-}ref}$, $i_{wd\text{-}ref}$	PWM current components of the *d*-axis and *q*-axis
C_f	grid-side filter capacitor
θ_g	grid phase
α	delay angle of CSI
m_a	amplitude modulation index
k_{ij}	transformer turn ratio
k_i	module average transformer turn ratio
k_{avg}	overall average transformer turn ratio
x_m	tolerance
θ_{1F}~θ_{4F}	fitted switching angles

List of Abbreviations

Symbol	Meaning
WECS	wind energy conversion system
MV	medium-voltage
LV	low-voltage
HVDC	high-voltage direct current
HVAC	high-voltage alternating current
CSC	current source converter
VSC	voltage source converter
LFT	low-frequency transformer
MFT	medium-frequency transformer
CSI	current source inverter
VSI	voltage source inverter
SHE	selective harmonic elimination
SVM	space vector modulation
CSR	current source rectifier
PMSG	permanent magnetic synchronous generator
MPPT	maximum power point tracking
PI	proportional-integral
VIR	voltage imbalance ratio
CIR	current imbalance ratio
PLL	phase lock loop
THD	total harmonic distortion

Chapter 1 Introduction

Offshore wind energy generation is increasing due to stronger and more stable wind sources. As the power rating and size of a single offshore wind turbine continue to increase [1], the deployment of ultra-high-power (10 MW plus) single wind turbines is becoming a growing trend.

Medium-voltage (MV) generators, with a voltage range of 3-4 kV, are more suitable for high-power wind energy conversion systems (WECS) due to lower copper losses and simplified installation compared to low-voltage (LV) generators, making MV operation of WECS a more economical and efficient approach, especially for power ratings over 3 MW [2], [3]. For a transmission distance of more than 50 kilometers, high-voltage direct current (HVDC) transmission is preferable to high-voltage alternating current (HVAC). Wind turbine connection methods are classified as parallel-connected and series-connected configurations. The current commercial offshore WECS mainly adopt the parallel-connected configuration, which is applied by ABB, Yaskawa, Siemens and other companies [4], [5]. However, the parallel configuration requires a bulky and costly offshore substation to house step-up transformers and converters. To address this issue, literature [6], [7], [8], [9], [10], [11], [12], [13], [14] propose the series-connected WECS to eliminate the need for the offshore substation, which can significantly reduce the cost and footprint, but there are still technical challenges in topologies, control schemes and modulation schemes.

This thesis proposes a novel series-connected current source converter (CSC)-based WECS. On the generator side, it combines an MV six-phase generator connected to two diode rectifiers with two medium-frequency transformer (MFT)-based modular converters on the generator side. On the grid side, it adopts dual-bridge current source inverters (CSIs). It features a smaller size and significantly mitigates the rotor torque ripple caused by the diode rectifier. In addition, the modular converter has voltage and current imbalance issues, so a corresponding control scheme is proposed. For CSIs, an

online selective harmonic elimination (SHE) modulation scheme is applied to significantly reduce memory usage.

This chapter introduces the existing series-connected CSC-based WECS, including low-frequency transformer (LFT)-based WECS and MFT-based WECS with the diode rectifier or the active rectifier. It introduces and compares two main modulation schemes for CSIs, including space vector modulation (SVM) and SHE. In addition, the existing issues in the introduced WECS are analyzed, and the dissertation objectives are proposed.

1.1 Series-Connected Current Source Converter-Based Configuration

The series-connected CSC-based WECS is a good candidate since it can eliminate the need for the offshore substation and offer variable DC-link voltage and reliable short-circuit protection. The pulse-width modulation (PWM) CSC-based configuration is shown in Fig. 1-1.

The generator is connected to the input of an AC-DC converter through an LFT. Then, the outputs of all AC-DC converters are connected in series to the HVDC transmission system. Another side of the transmission system is connected to multiple CSIs in series, and their outputs are connected to the national grid through the transformer.

However, in a series-connected configuration, the generator farthest from the ground point must endure the highest DC voltage, necessitating a transformer to isolate the generator from the high DC voltage. The transformer can be classified into the LFT and MFT according to operation frequency.

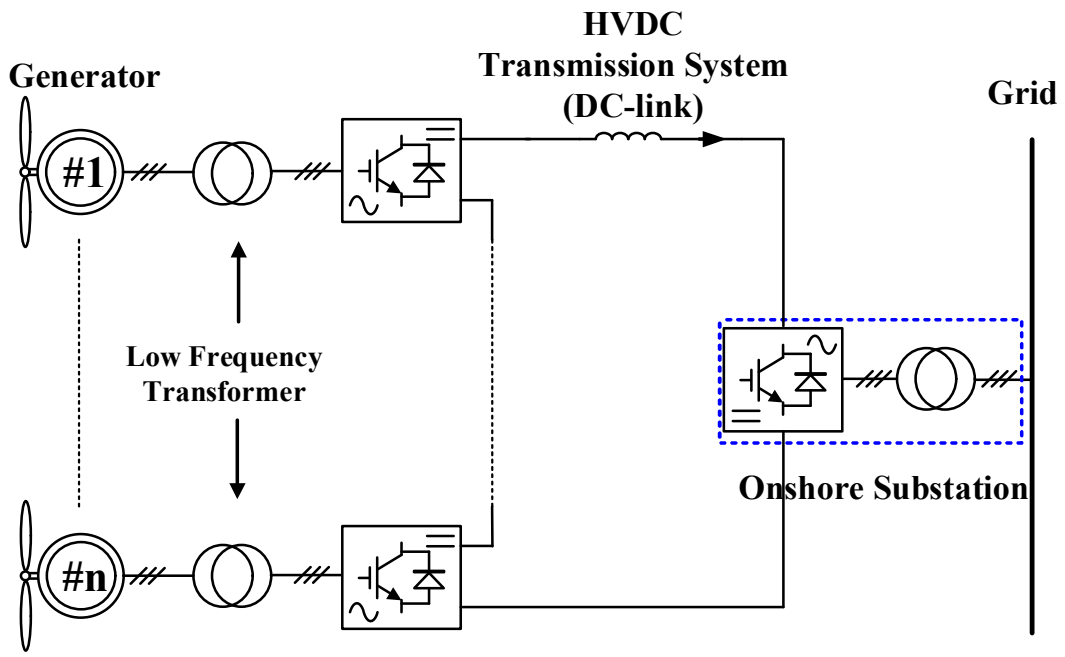

Fig. 1-1 A typical series-connected PWM CSC-based offshore wind farm configuration.

1.2 LFT-Based WECS

Literature [15] proposes an LFT-based WECS with the six-phase generator, shown in Fig. 1-2, which has a cascaded structure on the generator side. The six-phase generator has two sets of three-phase stator windings connected to two 2-level VSCs through two LFTs on the generator side.

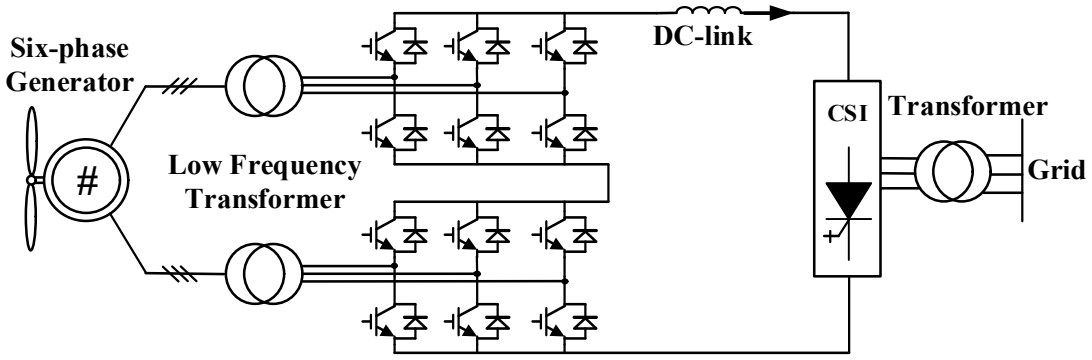

Fig. 1-2 LFT-based WECS with the six-phase generator.

Literature [16] proposes an LFT-based WECS with the three-phase generator, shown in Fig. 1-3, which has a back-to-back structure. It consists of the PWM current source rectifier (CSR) and CSI. The capacitor banks are used to assist in the commutation of switches and also reduce harmonics.

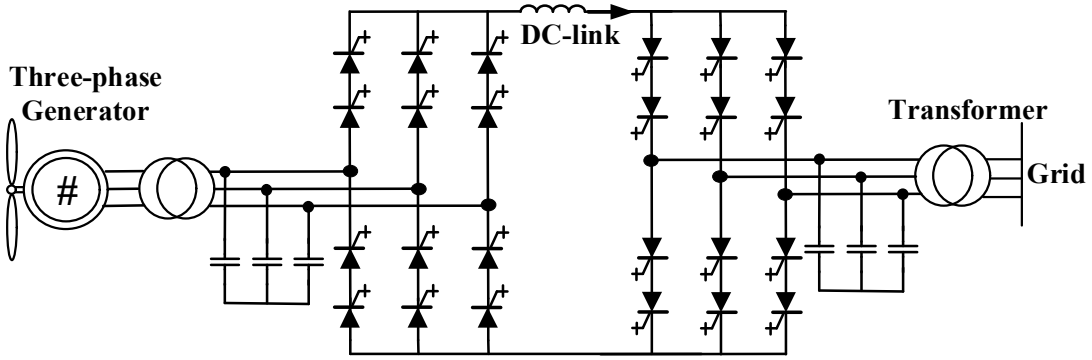

Fig. 1-3 LFT-based WECS with the three-phase generator.

However, the LFT has a large footprint and weight due to low operation frequency. Compared with the LFT, the MFT has a smaller size and weight, which is beneficial to the maintenance and installation in offshore WECS.

1.3 MFT-Based WECS

In the MFT-based WECS, the active rectifier or diode rectifier is adopted. The MFT-based WECS with the active rectifier is proposed [17], shown in Fig. 1-4. On the generator side, it utilizes the 2-level voltage source converter (VSC) as the rectifier to offer superior generator stator current harmonics performance and adopts the input series MFT-based modular converter. On the grid side, it adopts conventional 2-level CSI.

However, compared with the active rectifier, the diode rectifier has a lower cost, smaller size, lighter weight, and higher efficiency and reliability since the active switch requires complicated drivers and has a shorter lifetime and a higher failure rate.

The previous study [9] introduces an MFT-based WECS with the diode rectifier,

shown in Fig. 1-5. On the generator side, a diode rectifier is connected to a DC-DC MFT-based H-bridge converter. On the grid side, a conventional 2-level CSI is utilized.

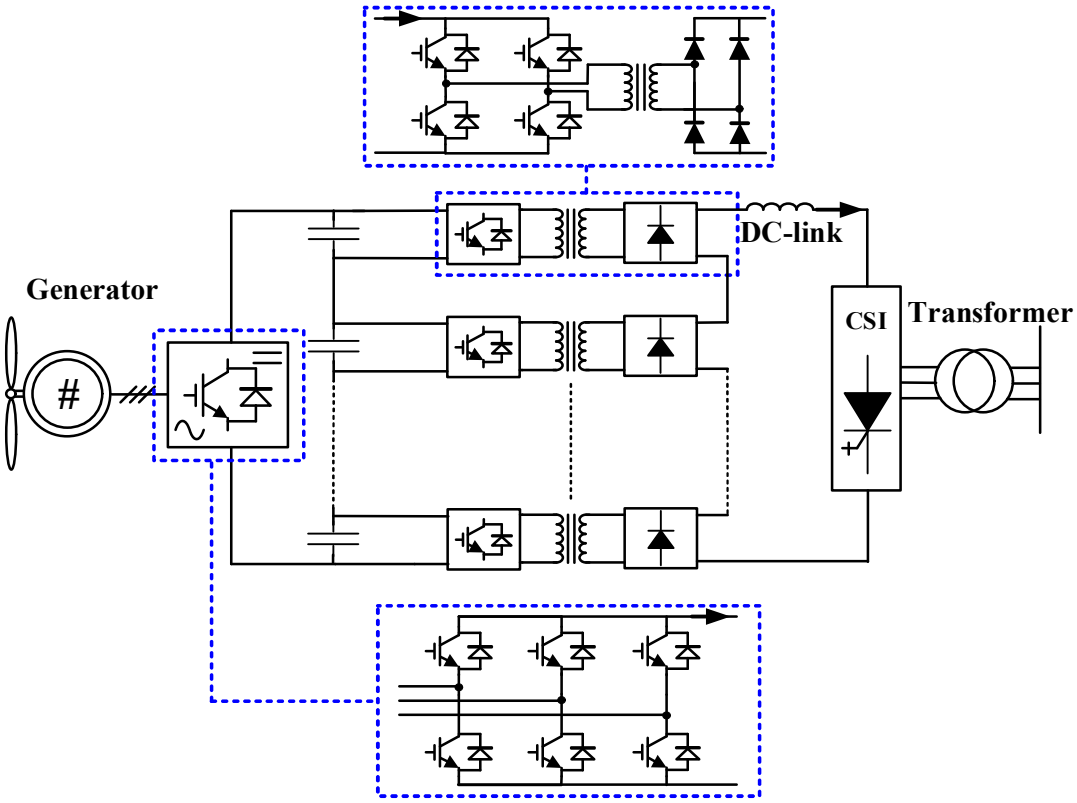

Fig. 1-4 MFT-based WECS with the active rectifier.

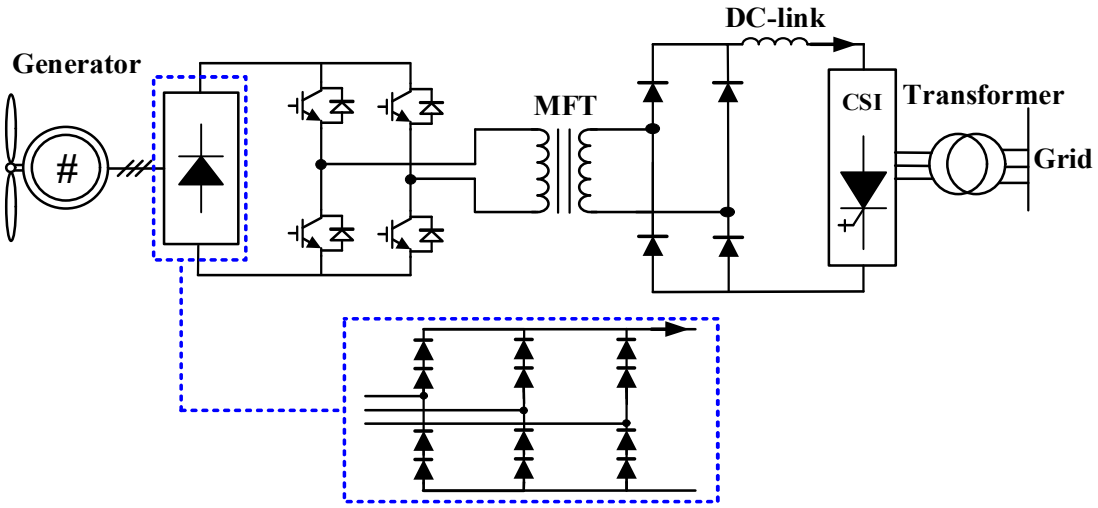

Fig. 1-5 WECS with the single MFT-based converter.

However, due to the immature technology, a single MFT encounters challenges related to insulation (transmission levels) and thermal design at high power levels (several MW). The main reason is that the MFT has difficulty in having a high insulation level and high power level at the same time. To address this issue, literature [10] proposes an MFT-based WECS, as shown in Fig. 1-6, which utilizes the input series MFT-based modular converter to substitute the single MFT-based converter.

This modular converter is composed of multiple MFT-based H-bridge converter modules. On the input side, several capacitors are connected in series, with each capacitor linked to an MFT-based H-bridge converter module. On the output side, the outputs of all H-bridge converter modules are connected in series to the DC-link. The converter employs multiple MFTs to distribute the high input power, enabling each MFT to handle only a portion of the total power. This topology allows the use of low-power MFT with mature technology in high-power WECS applications.

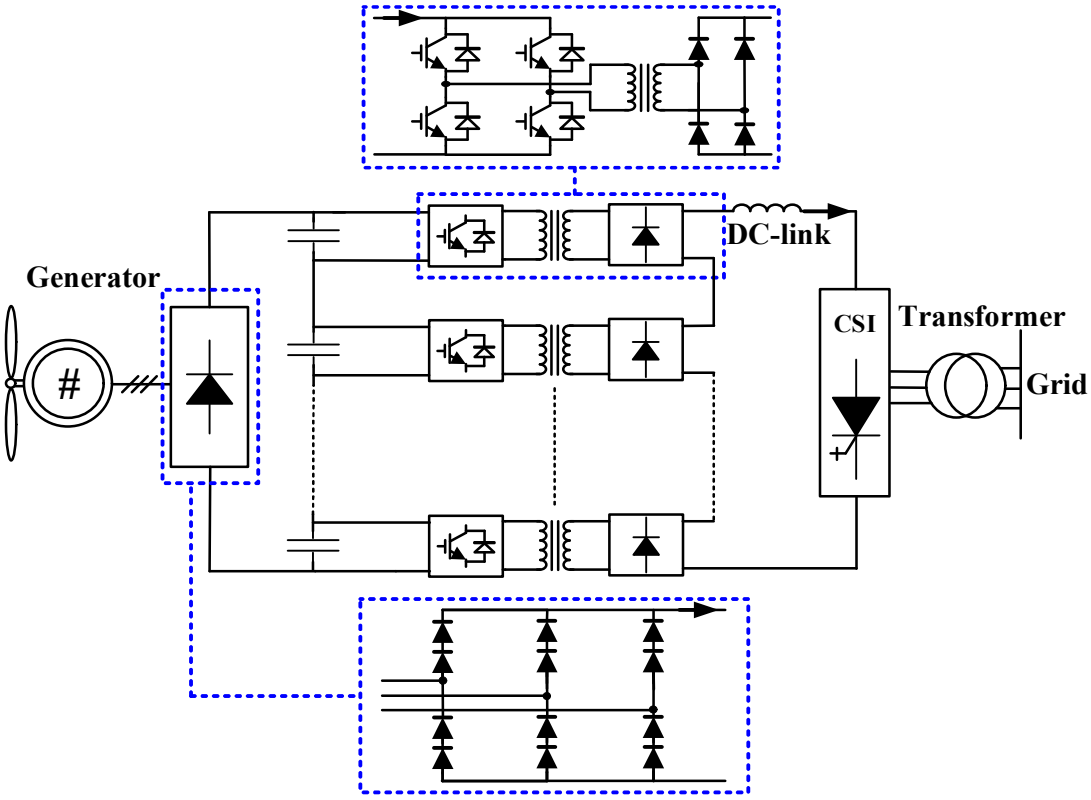

Fig. 1-6 WECS with the input series MFT-based modular converter.

However, at an ultra-power level (over 10 MW), the WECS of Fig. 1-6 still faces challenges. First, each MFT must handle a higher power level, increasing manufacturing complexity and technological demands. Second, as the power increases, so does the output current of the converter, which can lead to higher transmission losses. Finally, the capacitance of input-series capacitors must be increased to maintain acceptable input voltage ripple levels, which adds to both the cost and the footprint of the converter.

Building on this, literature [11] proposes an input series and parallel MFT-based modular converter, as shown in Fig. 1-7, constituted by more MFT-based H-bridge converter modules.

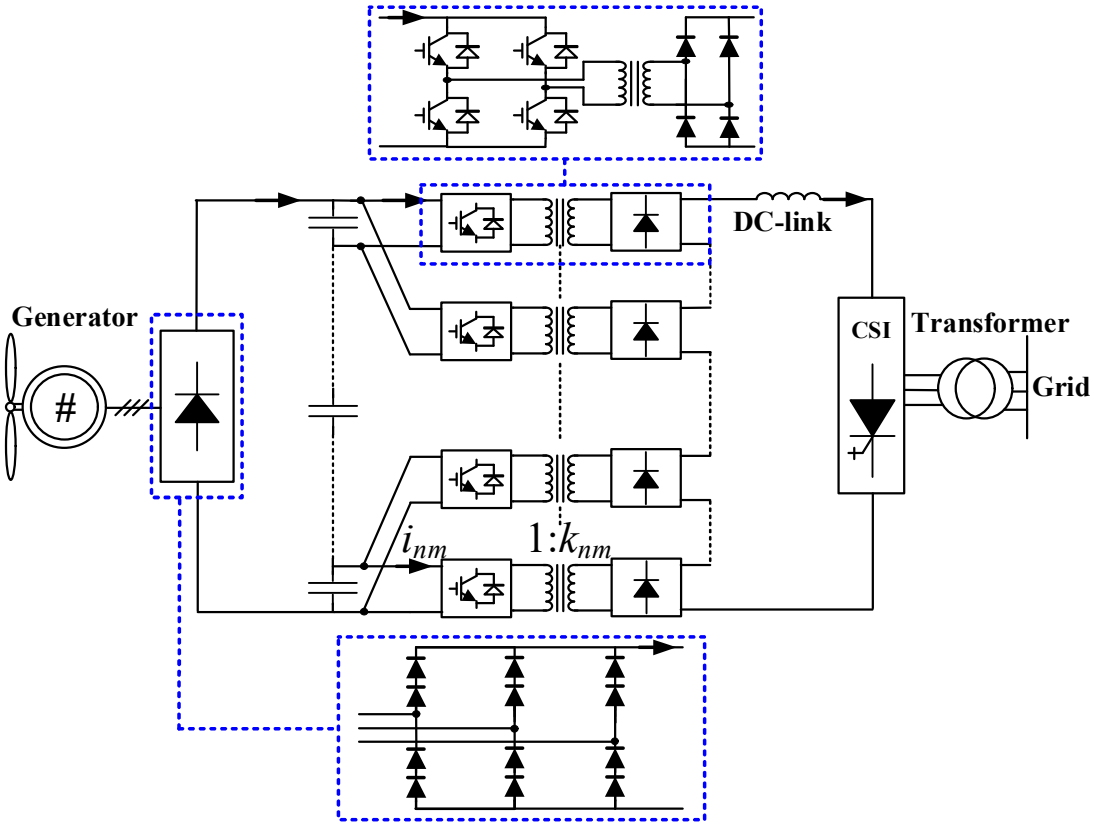

Fig. 1-7 WECS with input series and parallel MFT-based modular converter.

On the input side, multiple capacitors are connected in series, and each capacitor is connected to multiple interleaved parallel MFT-based H-bridge converters. On the

output side, it also has the same series structure. This modular converter offers several key advantages: 1) reduced manufacturing burden due to lower power demand on individual MFT; 2) increased voltage gain leading to higher transmission efficiency; and 3) smaller capacitances of input series capacitors due to multiple interleaved parallel H-bridge modules.

However, these existing MFT-based WECS with diode rectifiers have the issue of high torque ripple in the generator's rotor caused by high harmonics in the generator's stator, shortening the generator's lifespan [18].

1.4 Modulation Scheme for the Current Source Inverter

On the grid side of the offshore CSC-based WECS, the current source inverter is utilized to control DC-link current and reactive power control. A conventional 2-level PWM CSI is shown in Fig. 1-8.

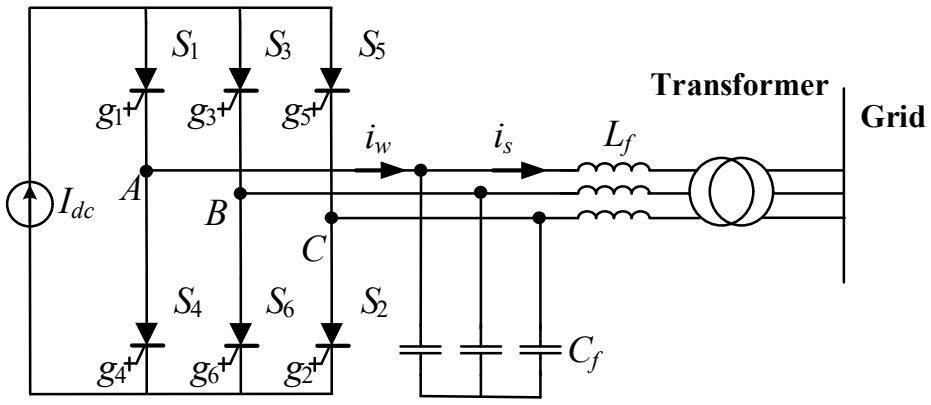

Fig. 1-8 A conventional 2-level PWM CSI.

In the figure, the input is the current source (I_{dc}). The outputs of CSI are connected to a three-phase capacitor (C_f) and inductance (L_f) to filter the harmonics of the inverter output current (i_w) so that the current flowing the national grid can meet the grid code compliance. For the CSC-based WECS, the DC-link with the huge inductance is regarded as a current source.

Compared with the voltage source inverter (VSI), the CSI has several advantages:

(1) Simple converter topology: Its switching devices do not need antiparallel free-wheeling diodes.

(2) Motor-friendly waveforms: The issue of high *dv/dt* does not exist because the DC-link inductance can constrain the current variation rate, reducing electromagnetic interference.

(3) Reliable short-circuit protection: When the short-circuit happens, the DC-link inductance can reduce the rate of rise of the DC current, which means that the protection circuit or program has sufficient time to function.

To ensure the operation of CSI, it must meet two conditions: (1) continuous input current (I_{dc}) and (2) definition of inverter output current (i_w). Therefore, the switching pattern should meet the switching constraint that there are only two conducting switches at any instant of time (excluding commutation intervals), and two switches are in the top half-bridge and the bottom half-bridge, respectively. In the CSC-based WECS, there are two main modulation schemes for CSC: SVM and SHE.

The SVM is widely investigated and used in the offshore CSC-based WECS [19], [20], [21], [22] due to its fast dynamic response. Based on the switching constraint of CSI, there are a total of nine switching states, which include six active switching states [12], [34], [45], [56], [61] and three zero switching states [14], [36], [52], shown in Table 1-1. The stationary space vectors corresponding to these switch states are plotted in Fig. 1-9.

In the space vector diagram, there are six sectors divided by six active vectors. The $\vec{I}_{ref}$ is the reference vector, which can be synthesized by three stationary vectors, which are the zero vector and two active vectors in the sector of the reference vector. The dwell times of these three stationery vectors directly decide the direction and amplitude of $\vec{I}_{ref}$ during a sampling period. The angular velocity (ω) of $\vec{I}_{ref}$ is equal to the electrical angular velocity of the CSI output current (i_w). Compared with SHE, SVM has better dynamic performance because its modulation index can be adjusted within a

sample period, and bypass operation (zero states) can directly control the (i_w).

Table 1-1 Switching states and space vectors

Type	Switching State	On-State Switch	Inverter PWM Current			Space Vector
			i_{wA}	i_{wB}	i_{wC}	
Zero States	[14]	S_1, S_4	0	0	0	$\vec{I}_0$
	[36]	S_3, S_6				
	[52]	S_5, S_2				
Active States	[61]	S_1, S_6	I_d	$-I_d$	0	$\vec{I}_1$
	[12]	S_1, S_2	I_d	0	$-I_d$	$\vec{I}_2$
	[23]	S_2, S_3	0	I_d	$-I_d$	$\vec{I}_3$
	[34]	S_3, S_4	$-I_d$	I_d	0	$\vec{I}_4$
	[45]	S_4, S_5	$-I_d$	0	I_d	$\vec{I}_5$
	[56]	S_5, S_6	0	$-I_d$	I_d	$\vec{I}_6$

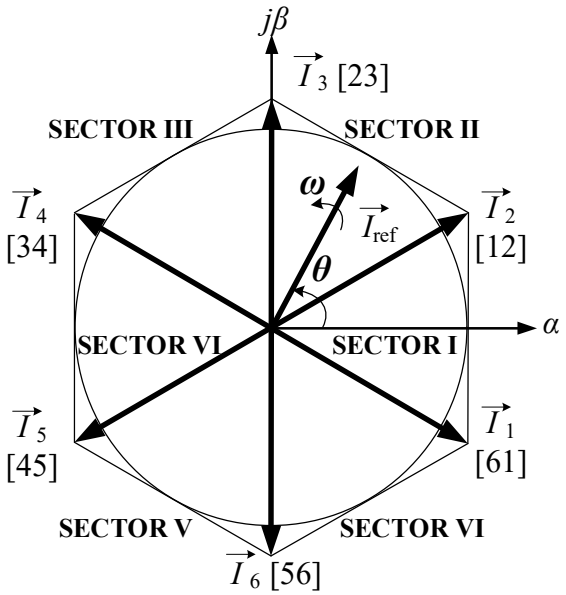

Fig. 1-9 Space vector diagram.

However, in the ultra-high-power WECS, excellent dynamic performance is unnecessary. The main reason is that significant turbine-generator system inertia causes input power to change relatively slowly. Hence, the DC-link current also slowly varies with the input power of wind turbines. Compared with SVM, SHE can achieve the same harmonic performance at a smaller switching frequency, thereby lowering switching losses or costs and the size of output filters [2], [23], [24], [25].

The SHE can completely eliminate several specific unexpected low-order harmonics in the inverter output current (i_w), which is achieved by pre-calculated switching angles in the look-up table stored in the digital controller. These switching angles are acquired by solving the Fourier coefficient equations. However, when demanding an adjustable amplitude modulation index, the convention SHE is an offline modulation. Pre-calculation of the switching angles is required to form a look-up stored in the digital controller. The lookup table can take in much of the digital controller's memory for high accuracy, causing increased costs.

1.5 Thesis Objectives

According to the above discussion, the LFT-based WECS face challenges of large size and weight due to using bulky LFT. The MFT-based WECS with the active switch has a higher cost, larger size and weight and lower reliability and efficiency than the diode rectifier. The MFT-based WECS with a diode rectifier faces challenges with high torque ripple in the generator rotor. On the grid side, conventional offline SHE modulation schemes for CSIs require significant memory resources because they rely on extensive look-up tables [26], [27], [28].

To address these challenges, the main objectives of this thesis are summarized as follows:

(1) Propose a novel CSC-based WECS: A novel CSC-based WECS is proposed, combining an MV six-phase generator connected to two diode rectifiers with two MFT-based modular converters on the generator and adopting dual-bridge CSIs

on the grid. It effectively mitigates the rotor torque ripple caused by the diode rectifiers and retains all the advantages of existing MFTs-based WECS. Additionally, a corresponding control scheme is proposed to address modular converters' voltage and current imbalance issues.

(2) Improve grid-side modulation: An online SHE modulation scheme is implemented for dual-bridge CSIs to significantly reduce the memory usage of the digital controller.

Chapter 2 Proposed Ultra-High-Power CSC-Based Wind Energy Conversion System

The existing MV CSC-based WECS face an issue of high rotor torque ripple due to the utilization of the diode rectifier, which is highly reliable and low-cost. To address this issue, a novel MV ultra-high-power CSC-based WECS is proposed.

In this chapter, the proposed configuration of WECS is introduced and analyzed. In addition, the modular converter's voltage and current imbalance issues are analyzed in detail. A corresponding control scheme is proposed. Finally, the proposed WECS is verified by the simulation.

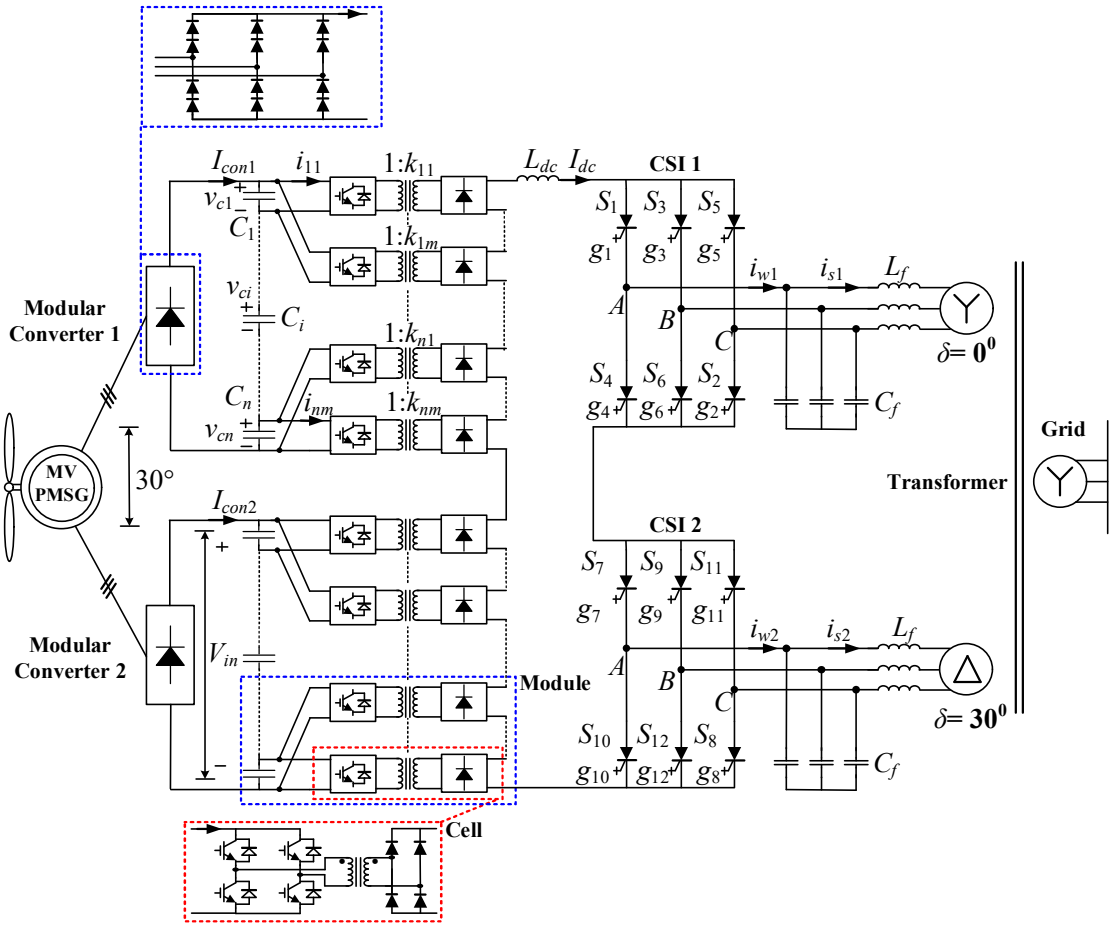

Fig. 2-1 Proposed MV ultra-high-power CSC-based WECS.

2.1 Configuration of Proposed CSC-Based Wind Energy Conversion Systems

The proposed MV ultra-high-power CSC-based WECS, as shown in Fig. 2-1, has a hybrid structure of VSCs on the generator side and CSCs on the grid side.

2.1.1 Generator-Side Configuration

The generator-side configuration consists of an MV six-phase permanent magnetic synchronous generator (PMSG) and two sets of a diode rectifier connected to an MFT-based modular converter.

The diode rectifiers generate significant harmonics, primarily low-order ones, which can result in high torque ripple and ultimately reduce the generator's lifespan. The six-phase PMSG has two sets of three-phase wye-connected windings, whose windings are separated by 30°. This configuration effectively eliminates the 5^{th} and 7^{th} harmonics of the equivalent currents of the stator magnetic field, thereby reducing torque ripple in the rotor and extending the generator's lifetime.

Each MFT-based modular converter has a structure of both series and parallel connections at the input and series connections at the output. The input terminal of the converter includes n series-connected capacitors (C_1, C_2, …., C_n) that share the input voltage, so the input voltage V_{in} is divided into n parts (v_{C1}, v_{C2}, …., v_{Cn}). Each capacitor is connected to inputs of m interleaved parallel cells, constituting a module, so the input current is also divided into m parts (i_{i1}, i_{i2}, …., i_{im}). Each cell comprises an H-bridge converter module with an MFT, and each H-bridge converter module has an active H-bridge on the primary side of the MFT and a diode H-bridge on the secondary side of the MFT. The output terminals of all cells are in series.

Therefore, each cell and MFT only handle $1/mn$ of rated power, which reduces the manufacturing burden of MFTs. The multiple interleaved parallel cells connected in each capacitor can effectively reduce the input current ripple, leading to lower

capacitance of the capacitor. In addition, the output series-connected structure significantly promotes the voltage gain, resulting in a high transmission efficiency.

A case study is provided to design the parameters of the MFT-based modular converter. The generator-side system parameters used in the study are presented in Table 2-1, where the V_{in} and I_{con1}/I_{con2} are the DC average voltage and current of each diode rectifier output.

Table 2-1 Generator-side system parameter

Item	Parameter	Item	Parameter
Rated Power	10 MW	Generator	PMSG, 3323V
V_{in}	4486 V	I_{con1}/I_{con2}	1115 A

For ultra-high-power applications, several factors determine the number n of modules and the number m of cells: 1) DC input voltage (V_{in}) and current (I_{in}); 2) the available IGBTs in the market; and 3) the power level of a single MFT. The turn ratios of the MFTs are set to 1:1 for good coupling because their main function is to isolate the generator from high voltage, so optimizing them is not the focus. Each MFT must withstand the maximum insulation voltage of the transmission level, but the technology of the MFT with simultaneous high power level and insulation level is immature. ABB designs the current commercial MFT with the highest power level, and each transformer has a capacity of 0.225 MW and a maximum insulation level of 75 kV [29], [30].

The design of the number of modules n and their cells m is tailored to the requirements of different applications, such as minimizing the cost and footprint, maximizing efficiency and achieving high fault tolerance. In this case study, the design primarily focuses on the minimum switch number. Considering voltage and current utilization and failure in time rate, the 1700 V-300 A IGBT is selected. As a result, for each modular converter, the number n of modules and the number m of cells are 5 and 6, respectively, and the number of the MFT is 30, so each MFT withstands 0.167 MW where the MFT has a mature technology.

With the improvement of the switching frequency, the size and weight of MFTs can be reduced, but the high switching frequency can cause the stress of thermal design and high losses due to the increased switching losses. Therefore, the switching frequency design should be a trade-off result. The switching frequency of the previously mentioned MFT designed by ABB is 1.2 kHz, so the switching frequency of the modular converters also adopts 1.2 kHz in this thesis.

2.1.2 Grid-Side Configuration

The grid-side configuration of the proposed WECS mainly comprises dual-bridge CSIs and a phase-shifting transformer. CSIs are connected to the national grid through the phase-shifting transformer.

The dual-bridge CSIs consist of two 2-level CSIs (CSI 1 and CSI 2) in series at the input, and their outputs are connected to a phase-shifting transformer through LC filters. In the phase-shifting transformer, its primary side has two sets of three-phase windings with wye-connection and delta-connection, which respectively introduce phase shifts of 0° and 30° for the input currents, and there is a set of wye-connected three-phase windings on the secondary side. Meanwhile, the switching signals of CSI 1 and CSI 2 are also phase-shifted by 0° and 30°, respectively.

This design eliminates the output current's 5th, 7th, 17th, and 19th harmonics. Additionally, two CSIs implement SHE to eliminate the 11^{th} and 13^{th} harmonics. Consequently, the output currents injected into the grid are free from harmonics below the 23rd order, which means low switching losses or low cost and size of filters.

2.2 Control Scheme

Based on the configuration of the proposed WECS, a corresponding control scheme diagram is proposed in Fig. 2-2. On the generator side, the control scheme mainly includes maximum power point tracking (MPPT) control and voltage balance control. There are the DC-link current control and the reactive power control on the grid side.

In the diagram, only the control scheme diagrams of Modular Converter 1 and CSI 1 are shown due to the same.

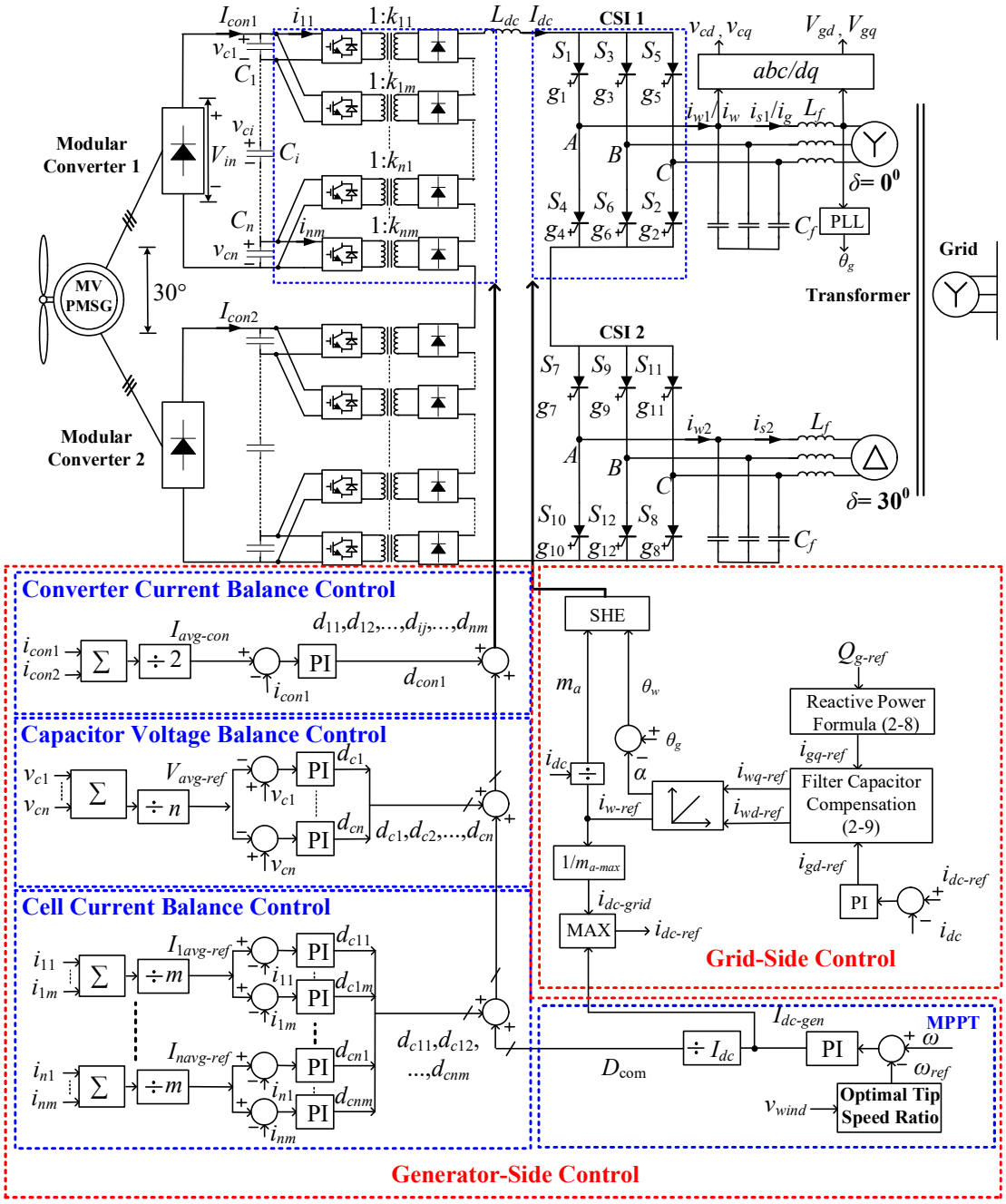

Fig. 2-2 Proposed control scheme diagram.

2.2.1 Generator-Side Control

Four control objectives must be achieved for the generator-side controls: MPPT, input capacitor voltage balance of each modular converter, cell current balance and converter balance. Two MFT-based modular converters implement these controls. They adopt the conventional PWM, where the duty cycles of switches range from 0 to 0.5. The up/down switch of one bridge arm shares the same switching signal as the down/up switch of another bridge arm of the H-bridge, with a phase difference of 180 degrees between the switching signals of the up and down switches within the same bridge arm. For the switches in the same position on different cells within the same module, the phase difference between their switching signals is 180/m degrees, which enables the interleaved parallel operation to reduce the input capacitance requirements of the input capacitors.

In a variable speed WECS, the modular converters adjust the generator speed to achieve MPPT. The control methods for MPPT, including optimal power profile, optimal tip speed ratio and optimal torque control, have been widely discussed in the literature [18]. Therefore, this thesis implements MPPT using the simple optimal tip speed ratio and current wind speed (v_{wind}) to acquire the generator speed reference (ω_{ref}). The error between this reference and the actual generator speed ω is processed by the wind speed proportional-integral (PI) controller to generate the generator-side DC-link current reference ($i_{dc\text{-}gen}$). Then, $i_{dc\text{-}gen}$ is divided by i_{dc} to get the duty cycle (D_{com}), which both modular converters share.

Despite an identical design, the series and parallel structure of the converter often encounters issues of unbalanced voltage and current due to inconsistent characteristics among its components. For modular converters, mismatches in transformer turn ratios are the primary factor influencing voltage and current imbalances [31]. Even slight mismatches in transformer turn ratios can lead to uneven power distribution among cells, resulting in increased losses and potential damage to the converter. Therefore, ensuring power balance is crucial for maintaining stability and high efficiency.

To mitigate this, a control scheme that simultaneously manages capacitor voltage

balance, cell current balance, and input converter current balance is implemented. The voltage and current imbalance caused by transformer turn ratios will be discussed and analyzed.

The voltage imbalance ratio (VIR) and current imbalance ratio (CIR) are defined as:

$$\begin{cases} VIR = \dfrac{|V_{max} - V_{avg}|}{V_{avg}} 100\% \\ CIR = \dfrac{|I_{max} - I_{avg}|}{I_{avg}} 100\% \end{cases}. \tag{2-1}$$

For this modular converter topology, V_{max} is the capacitor voltage with a maximum deviation from the average voltage of all capacitors (V_{avg}). The currents between modules are balanced and equal to I_{con1} due to the structure of the input series connection. However, within the same module, the input average currents between cells may become unbalanced because of the input parallel-connected structure and parameter mismatches. For a module, the I_{max} is the cell input current with a maximum deviation from the average current (I_{avg}) of cells connected to the same capacitor. For two modular converters, the (I_{max}) is the input current of the modular converter with a maximum deviation from the average current of two modular converters. The following section will analyze the voltage and current imbalance ratios in detail.

As transformer turn ratios are set as 1:1 for well-coupling, these transformers have a small leakage inductance, which means the differences among leakage inductances are quite small. This paper assumes all transformers have the same leakage inductance (L_{lk}). Based on the law of conservation of charge, we derive formula (2-2) without consideration of balance control. In the formula (2-2), k_{ij} represents the transformer turn ratio from secondary to primary, and T is the switching period. From formula (2-2), the total voltage across the input series capacitors equals the input voltage (V_{in}), which remains constant under fixed wind speed conditions, as does the output current (I_{con1}).

$$\begin{cases} \sum_{j=1}^{m}[i_{1j}] = 2\sum_{j=1}^{m}[D_{com}TI_{dc}k_{1j} - \dfrac{I_{dc}^2 k_{1j}^2 L_{lk}}{v_{c1}}] = I_{con1}T \\ \sum_{j=1}^{m}[i_{2j}] = 2\sum_{j=1}^{m}[D_{com}TI_{dc}k_{2j} - \dfrac{I_{dc}^2 k_{2j}^2 L_{lk}}{v_{c2}}] = I_{con1}T \\ \qquad\qquad \ldots\ldots \\ \sum_{j=1}^{m}[i_{nj}] = 2\sum_{j=1}^{m}[D_{com}TI_{dc}k_{nj} - \dfrac{I_{dc}^2 k_{nj}^2 L_{lk}}{v_{cn}}] = I_{con1}T \\ v_{c1} + v_{c2} + \ldots\ldots + v_{cn} = V_{in} \end{cases} . \tag{2-2}$$

Therefore, VIR is determined by the overall average turn ratio (k_{avg}) and the average transformer turn ratio ($k_{i\text{-}max}$) with a maximum deviation from k_{avg}. If the k_i is less than the k_{avg}, the input capacitor voltage (v_{ci}) will be above the average capacitor voltage and vice versa. In other words, the further k_i deviates from k_{avg}, the more the corresponding capacitor voltage (v_{ci}) deviates from the average value. Consequently, within a given range of transformer turn ratios [(1-x) k, (1+ x) k], where k represents the theoretical value of the transformer turn ratio, and x represents the tolerance of the transformer turn ratio, the maximum/minimum v_{ci} occurs when one module has its turn ratio k_i at the lower limit (1-x) k / upper limit (1+x) k, while the turn ratios of the other modules are at the upper limit (1+x) k / lower limit (1-x). The maximum VIR is acquired when the condition of the maximum v_{ci} is substituted into the formula (2-2), and then we derive formula (2-3) to get the maximum VIR and v_{C1}.

$$\begin{cases} D_{com}TI_{dc}m(1-x)k - \dfrac{I_{dc}^2 L_{lk} m(1-x)^2 k^2}{v_{c1}} = \dfrac{I_{con1}T}{2} \\ D_{com}TI_{dc}m(1+x)k - \dfrac{I_{dc}^2 L_{lk} m(1+x)^2 k^2}{v_{c2}} = \dfrac{I_{con1}T}{2} \\ \qquad\qquad \ldots\ldots \\ D_{com}TI_{dc}m(1+x)k - \dfrac{I_{dc}^2 L_{lk} m(1+x)^2 k^2}{v_{cn}} = \dfrac{I_{con1}T}{2} \\ v_{c1} + v_{c2} + \ldots\ldots + v_{cn} = V_{in} \end{cases} . \tag{2-3}$$

In the (2-3), the average turn ratio of the 1st module takes the lower limit, and others take the upper limit. As the acceptable VIR range is within ±1% in the industry to ensure the longevity and reliability of the system components, the maximum v_{ci} is set as

$1.01V_{avg}$, which is substituted into formula (2-3), yielding formula (2-4) to calculate the tolerance (x_m). The VIR is less than 1% when the transformer turn ratio is within the range of [(1- x_m) k, (1+ x_m) k], while voltage balance control becomes necessary when the turn ratio exceeds this range.

$$\begin{cases} v_{c1} = \dfrac{2I_{dc}^2 L_{lk} m(1-x_{\max})^2 k^2}{2D_{com} T I_{dc} m(1-x_{\max})k - I_{con1} T} = 1.01V_{avg} \\ \dfrac{2I_{dc}^2 L_{lk} m(1-x_{\max})^2 k^2}{2D_{com} T I_{dc} m(1-x_{\max})k - I_{con1} T} + \dfrac{2I_{dc}^2 L_{lk} m(n-1)(1+x_{\max})^2 k^2}{2D_{com} T I_{dc} m(1+x_{\max})k - I_{con1} T} = V_{in} \end{cases} . \quad (2\text{-}4)$$

By applying the mentioned case study parameters to the (2-4), x_m is calculated to be 0.001, namely 0.1%. However, according to IEEE C57.12.00-2020 [32], the turn ratio tolerance of two-winding transformers is generally within ± 7.5%, so the tolerance is set at ± 10% in this thesis, considering a certain margin.

Therefore, implementing capacitor voltage balance control is essential to ensure system stability and performance. In terms of the capacitor voltage balance control, the average voltage of all capacitors in a modular converter is used as the reference $V_{avg\text{-}ref}$, and the difference between the average voltage and each capacitor voltage is processed through the voltage balance PI controller to generate the control signal d_{ci} for all cells within the ith module.

According to the previous analysis, the discussion of the current imbalanced situations is classified into the case between cells within the same module and between two modular converters.

For the current imbalance between cells, the input average current ($i_{cell\text{-}avg}$) of each cell is expressed in formula (2-5):

$$i_{cell-avg} = 2I_{dc}k_{ij}(d - \frac{I_{dc}k_{ij}L_{lk}}{Tv_{ci}}). \quad (2\text{-}5)$$

In the formula, d represents the duty cycle of switches. As the transformer leakage inductance (L_{lk}) is quite small, the (2-5) can be further simplified into the (2-6).

$$i_{cell-avg} = 2I_{dc}k_{ij}d . \quad (2\text{-}6)$$

The $i_{cell\text{-}avg}$ is proportional to the transformer turn ratio k_{ij} because the transformer

leakage inductance (L_{lk}) is quite small in a well-coupled transformer. Therefore, the CIR is determined by the module average transformer turn ratio k_i and the k_{ij} with the maximum deviation from k_i.

Based on the above analysis, for the transformer with turn ratio tolerance ±10%, the worst imbalance situation of the cell current is when a cell's transformer turn ratio is in the tolerance upper limit value of 1.1, but the remaining turn ratios are in the lower limit of 0.9. As a result, the maximum CIR of the cell current is 17.86%. The CIR is required within ±5% to avoid overheating and ensure stable operation in the industry. Consequently, the cell's current balance control must be implemented.

For the current imbalance between modular converters, the modular converter input average current i_{con1} is expressed as:

$$i_{con1} = 2dI_{dc}\sum_{j=1}^{m}[k_{ij}] = 2D_{com}I_{dc}mk_{avg}\,. \tag{2-7}$$

The modular converter input average current is also proportional to the average k_{avg} of all transformer turn ratios in that converter. The worst imbalance condition of the modular converters is when the average turn ratio of a modular converter is in the upper limit of 1.1, but another one is in the lower limit of 0.9. It will also cause overheating.

Consequently, the balance control scheme, including capacitor voltage balance control, cell current balance control and converter current balance control, must be implemented to address the voltage and current imbalance issues in modular converters to meet industry standards. According to the above analysis, the input series structure determines the same input current for modules within the same converter, while the transformer turn ratio distribution determines the input current of cells within the same module and the modular converters, and each modular converter has the same input voltage. Therefore, the voltage control and current controls are decoupled, which means the proposed control scheme can effectively address unbalanced voltage and current issues.

2.2.2 Grid-Side Control

On the grid side, the control objectives are the DC-link current control and the reactive power control, both implemented through dual-bridge CSIs using the SHE modulation scheme. The DC-link current control regulates wind energy transmission. Meanwhile, reactive power control ensures that the energy transmitted to the grid complies with the grid code.

The current control of the DC-link plays a crucial role in the entire WECS since it determines the efficiency and dynamic performance of the system [29], [30]. The DC-link current control can be classified into fixed and variable current control. The fixed current control has a good dynamic performance, but it can cause high transmission losses, lowering the efficiency of the overall system, especially in the condition of low wind speed. In contrast, the variable current control has a high efficiency but at the expense of poor dynamic performance. Therefore, the efficiency and dynamic performance of the system are coupled.

In variable DC-link current control, the DC-link current adjusts according to the input wind energy, maintaining it at an optimal minimum where all control objectives are met and the system operation remains highly efficient. In the ultra-high-power WECS, the huge inertia of the turbine-generator system enables the DC-link current to change slowly. Additionally, system efficiency is prioritized over dynamic performance in wind farms. Therefore, the variable DC-link current control is a more cost-effective and suitable approach for the ultra-high-power WECS.

The filter capacitor voltage (v_c) and the grid-side voltage (V_g) are measured and transformed from stationary frame *abc*-axis to *dq*-axis, so their components of the *d*-axis and *q*-axis are v_{cd}, v_{cq} and V_{gd}, V_{gq}. The reactive power transmitted into the grid is expressed by:

$$Q_{g-ref} = 1.5 V_{gd} i_{gq-ref} . \tag{2-8}$$

The *q*-axis components of the current transmitted into the grid ($i_{gq\text{-}ref}$) are calculated using the formula (2-8) and the grid reactive power reference ($Q_{g\text{-}ref}$) from the grid code.

The *d*-axis component of the current ($i_{gd\text{-}ref}$) is generated by the DC-link current PI controller, which uses the error between the DC-link current reference ($i_{dc\text{-}ref}$) and the actual DC-link current (i_{dc}) as its input. The PWM current components of the *d*-axis and *q*-axis are $i_{wq\text{-}ref}$ and $i_{wd\text{-}ref}$, respectively, which are obtained by the filter capacitor compensation formula:

$$\begin{cases} i_{wd-ref} = i_{gd-ref} + i_{cd} = i_{gd-ref} - \omega_g C_f V_{cq} \\ i_{wq-ref} = i_{gq-ref} + i_{cq} = i_{gq-ref} + \omega_g C_f V_{cd} \end{cases}, \tag{2-9}$$

where the filter capacitor (C_f) and the ω_g is the electrical angular velocity of the grid, the ω_g is transformed by the grid phase (θ_g) generated by the phase lock loop (PLL). Then, based on the $i_{wq\text{-}ref}$ and $i_{wd\text{-}ref}$, the PWM current and delay angle α of CSI are obtained by:

$$\begin{cases} i_{w-ref} = \sqrt{i_{wd-ref}^2 + i_{wq-ref}^2} \\ \alpha = \arctan(i_{wq-ref} / i_{wd-ref}) \end{cases}. \tag{2-10}$$

The real amplitude modulation index m_a and PWM current angle (θ_w) of SHE modulation output are obtained by:

$$\begin{cases} m_a = i_{w-ref} / i_{dc} \\ \theta_w = \theta_g - \alpha \end{cases}. \tag{2-11}$$

The DC-link current reference is determined by both grid-side and generator-side controls to ensure that it simultaneously satisfies MPPT and DC-link current control objectives at a minimum value. As previously mentioned, the generator-side DC-link current reference ($i_{dc\text{-}gen}$) is generated through the wind speed PI controller. The grid-side DC-link current reference ($i_{dc\text{-}grid}$) is calculated using the following formula:

$$i_{dc-grid} = i_{w-ref} / m_{a-\max}, \tag{2-12}$$

where the $m_{a\text{-}max}$ is the maximum amplitude index of SHE modulation, and the maximum amplitude index means the highest DC current utilization ratio, resulting in the smallest DC-link current and the highest transmission efficiency. The final DC-link current reference ($i_{dc\text{-}ref}$) is determined as the larger value between $I_{dc\text{-}gen}$ and $I_{dc\text{-}grid}$.

2.3 Simulation Results

The feasibility of the proposed WECS and corresponding control schemes have been verified by the simulation results based on MATLAB/Simulink. The simulations include (1) the comparative simulations with and without balanced control to verify voltage balance control and current imbalance analysis and (2) the stepped input wind speed simulation to evaluate the dynamic performance of the proposed WECS.

Table 2-2 WECS system parameter

MV Six-phase PMSG		System Rating	
Synchronous Inductance	0.4 pu	Nominal Power	10 MW
Stator Resistance	0.01 pu	Nominal Grid Voltage	4160 V
Rated Generator Voltage	3323 V	Frequency	60 Hz

The wind turbine and PMSG are modelled using components from the Simulink library, while linear transformer models represent the MFTs. The grid is simulated using a three-phase voltage source as a substitute. The WECS parameters are shown in Table 2-2, which is the same as the previous case study. The generator parameters are expressed based on the per-unit system. The simulation waveforms are shown based on the per-unit system, and the input DC voltage V_{in} and current I_{con1} are respectively set as base voltage and current.

The modular converter parameters are based on the previous case study's design results, shown in Table 2-3. The MFTs are divided into five teams (1) ~ (5), respectively, applied to modules 1 ~ 5 where $C_1 \sim C_5$ is located. To simulate the maximum deviation between input capacitor voltages, the turn ratios are the same within the same module, and there is a 5% difference between modules. For the simulation of maximum deviation between the cell currents, the average turn ratios are the same between modules, and there is a 2% difference between turn ratios within the same module. For the worst current imbalance simulation between the modular converters, the

transformer turn ratios of Modular Converter 1 and Modular Converter 2 are set as 1:1.1 and 1:0.9, respectively.

Table 2-3 Modular converter parameter

Module Number	5	Input Series Capacitor C_n	3 mF
Cell Number	6	Switching Frequency	1.2 kHz
Medium-Frequency Transformers			
Transformer Turn Ratio	Voltage Imbalance Simulation		Current Imbalance Simulation
(1) k_{11}~ k_{16}	1:0.90/1:0.90/1:0.90/ 1:0.90/1:0.90/1:0.90		1:0.90/1:0.94/1:0.98/ 1:1.02/1:1.06/1:1.1
(2) k_{21}~ k_{26}	1:0.95/1:0.95/1:0.95/ 1:0.95/1:0.95/1:0.95		1:0.90/1:0.94/1:0.98/ 1:1.02/1:1.06/1:1.1
(3) k_{31}~ k_{36}	1:1/1:1/1:1/ 1:1/1:1/1:1		1:0.90/1:0.94/1:0.98/ 1:1.02/1:1.06/1:1.1
(4) k_{41}~ k_{46}	1:1.05/1:1.05/1:1.05/ 1:1.05/1:1.05/1:1.05		1:0.90/1:0.94/1:0.98/ 1:1.02/1:1.06/1:1.1
(5) k_{51}~ k_{56}	1:1.1 /1:1.1/1:1.1/ 1:1.1/1:1.1/1:1.1		1:0.90/1:0.94/1:0.98/ 1:1.02/1:1.06/1:1.1

Fig. 2-3 shows the rotor torque ripple comparison between the six-phase generator and the three-phase generator in the same capacity (10 MW). The three-phase generator adopts the configuration of Fig. 1-7, where the generator is connected to a diode rectifier and a modular converter. Fig. 2-3 (a) shows that the rotor torque ripple of the six-phase generator has torque ripple 4250 N·m, and the three-phase generator is 10160 N·m, as shown in Fig. 2-3 (b). Therefore, the six-phase generator effectively mitigates the rotor torque ripple.

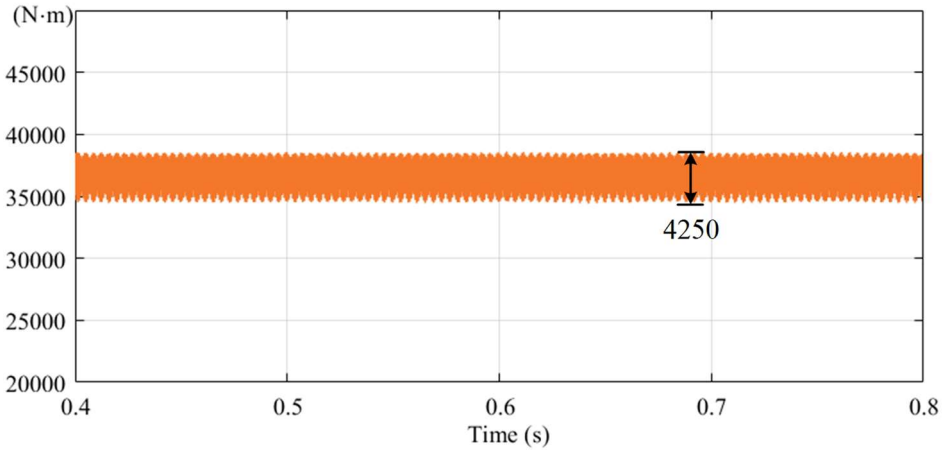

(a) Six-phase generator

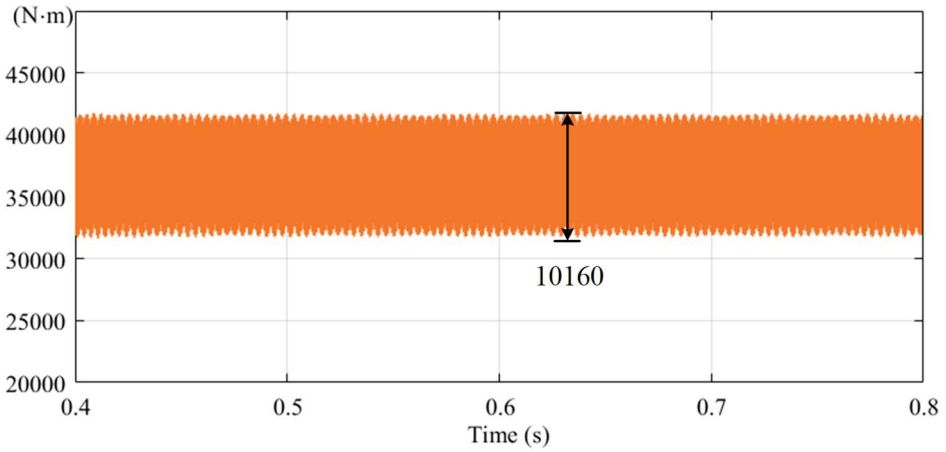

(b) Three-phase generator

Fig. 2-3 Comparative simulations in the six-phase and the three-phase generator.

Fig. 2-4 shows the spectrums of stator current i_{con1_a}, i_{con2_a} and the equivalent current of the stator magnetic field. The equivalent current of the stator magnetic field is equal to the sum of i_{con1_a} and i_{con2_a}. In Fig. 2-4 (a) and (b), the 5th and 7th harmonics of the stator current (i_{con1_a}) divided by the fundamental wave are 42% and 16%, respectively, the same as i_{con2_a}. Their total harmonic distortions (THD) are 45.14% and 45.72%. However, the 5th and 7th harmonics of the equivalent current of the stator magnetic field divided by the fundamental wave are mitigated to 1.5% and 0.8%, respectively, while the THD is also reduced to 4.15%. Therefore, the proposed configuration can significantly mitigate the rotor torque ripple.

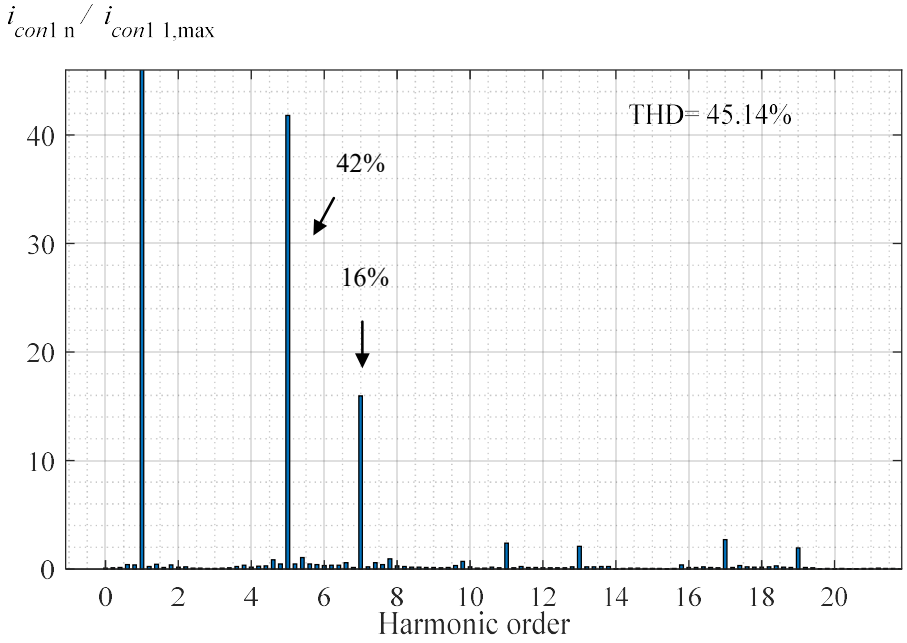

(a) Spectrums of stator current i_{con1_a}

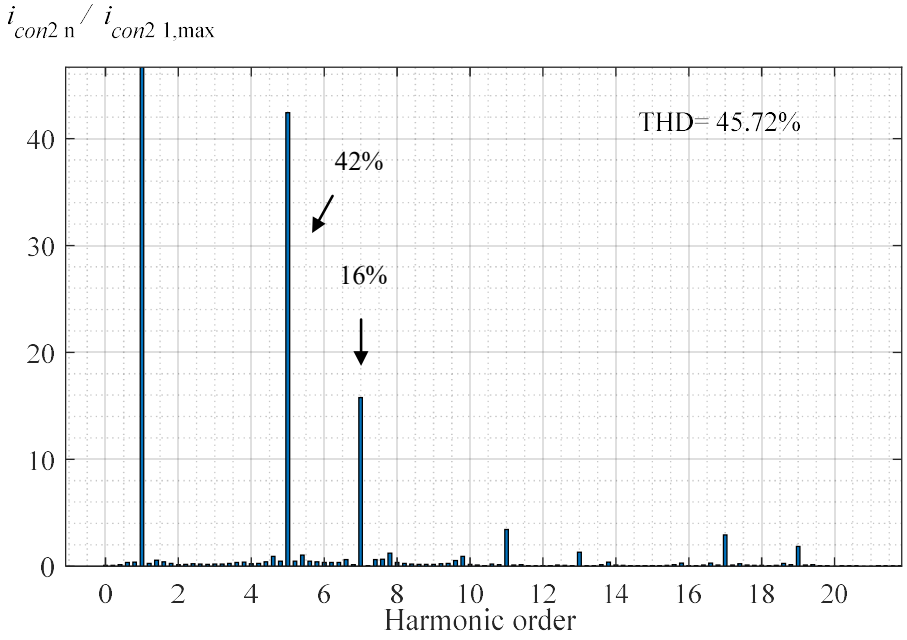

(b) Spectrums of stator current i_{con2_a}

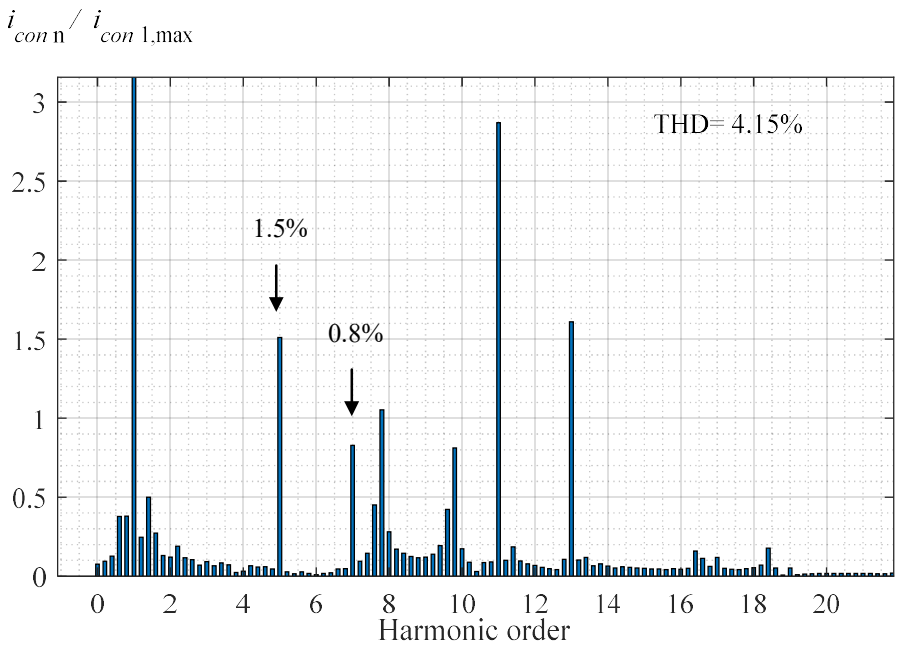

(c) Spectrum of equivalent current of the stator magnetic field

Fig. 2-4 Spectrum of stator current i_{con1_a}, i_{con2_a} and the equivalent current of the stator magnetic field.

The comparative simulations with and without balanced control are illustrated in Fig. 2-5. Specifically, Fig. 2-5 (a) (b) (c) respectively show the input capacitor voltages of Modular Converter 1 (v_{C1}, v_{C2}, …., v_{Cn}), cell input average currents of Module 1 (i_{11}, i_{12}, …., i_{16}) and modular converter currents (i_{con1}, i_{con2}). In Fig. 2-5 (a), voltage balance control is enforced during the period from 0.4 s to 0.8 s. All input capacitor voltages are well balanced at 0.2 pu, so VIR is zero. However, from 0.8 s to 1.2 s, when the balance controls are deactivated, the input capacitor voltages vary due to transformer turn ratio differences. The maximum voltage deviation is approximately 0.22 pu from v_{C1} to V_{avg} (0.2 pu), resulting in a VIR of 110%. When balance control is reactivated between 1.2 s and 1.6 s, the capacitor voltages quickly restore to a balanced state.

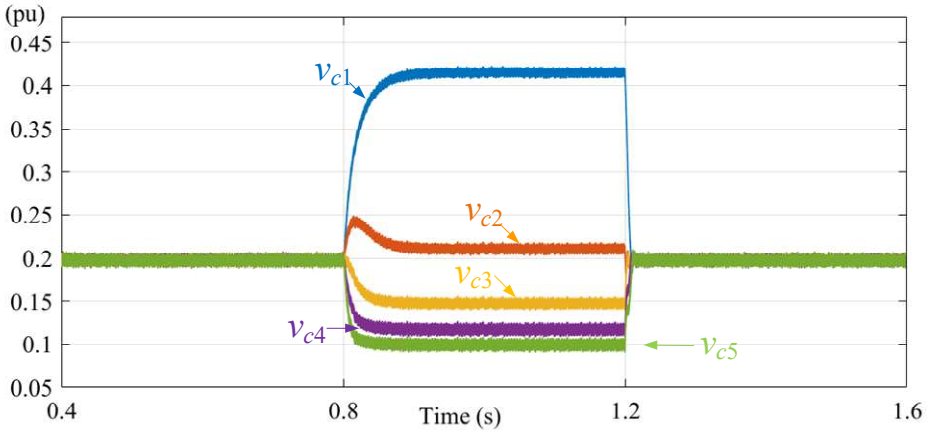

(c) Input capacitor voltages of Modular Converter 1

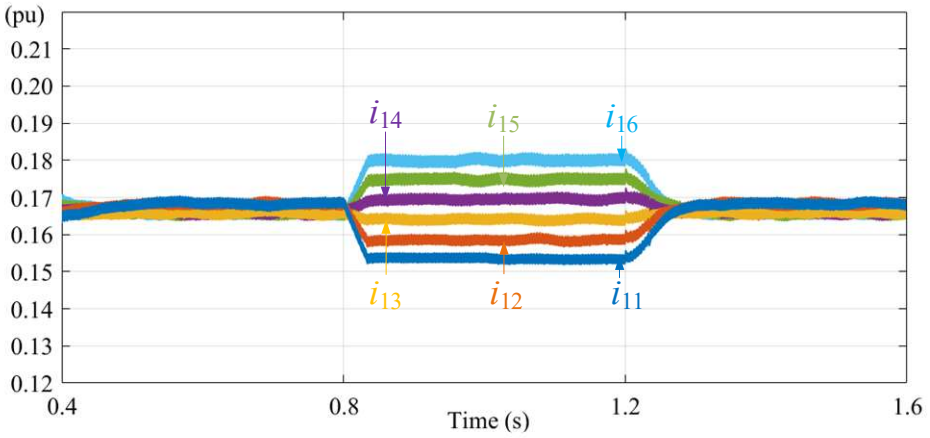

(d) Cell input average currents of Module 1

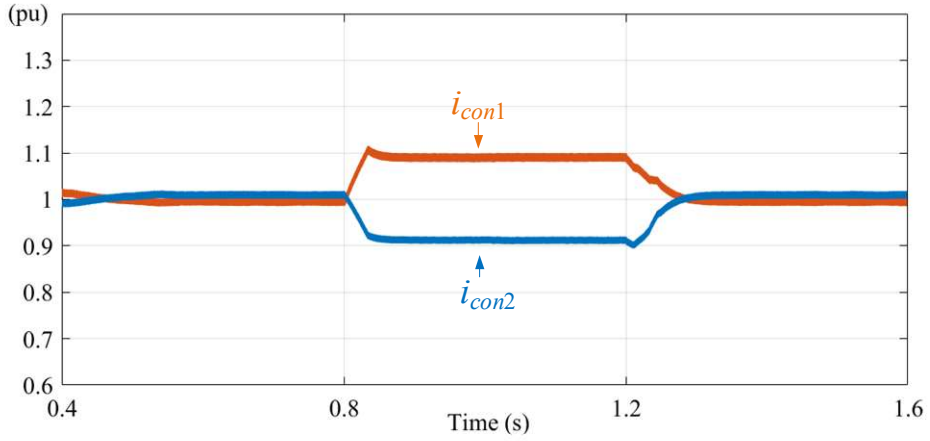

(e) Modular converter currents

Fig. 2-5 Comparative simulations with and without balanced control.

As shown in Fig. 2-5 (b), during the time without current balance control, the maximum deviation from I_{avg} (0.167 pu) is approximately 0.013 pu, leading to a cell CIR of 7.78%. Similarly, the maximum deviation of modular converter currents, shown in Fig. 2-5(c), is 0.1 pu, corresponding to a CIR of 10%. These results prove that CIR is proportional to transformer turn ratio distribution. During the time with current balance control, the cell current and converter current are in the balance state. These simulation results demonstrate that the proposed balance control scheme effectively addresses voltage and current balance issues in modular converters, ensuring capacitor voltage balance.

Fig. 2-6 presents the stepped input wind speed simulations, where the wind speed step down from 12 m/s (1 pu) to 10 m/s (0.83 pu) at t = 0.7 s and then step up from 10 m/s to 12 m/s at t=1.2 s. Meanwhile, the captured wind energy varies from 1 pu and 0.57 pu and then back to 1 pu. The captured wind energy has a cubic function with generator speed. Fig. 2-6 (a) shows that the generator speed is dynamically adjusted to capture maximum wind energy by the MPPT control, and the generator speed ω can closely track the reference ω_{ref}. From Fig. 2-6 (b) (c) (d), the voltage and current maintain a good balance during the variation of wind speed.

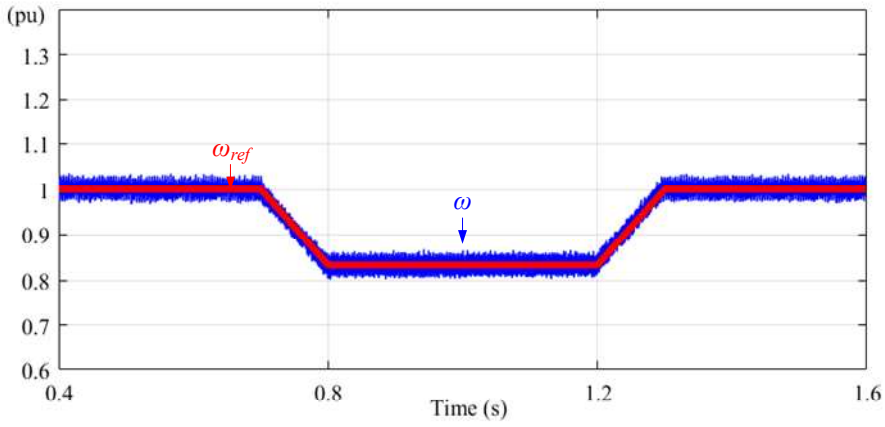

(a) Generator speed

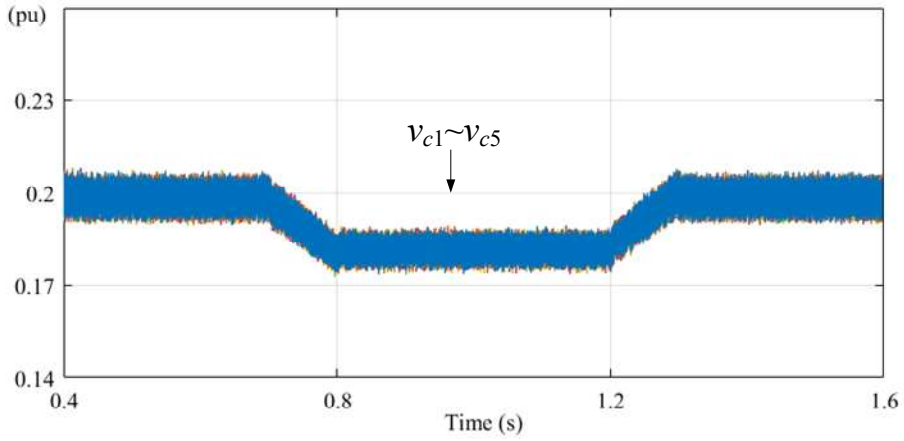

(b) Input capacitor voltages of Modular Converter 1

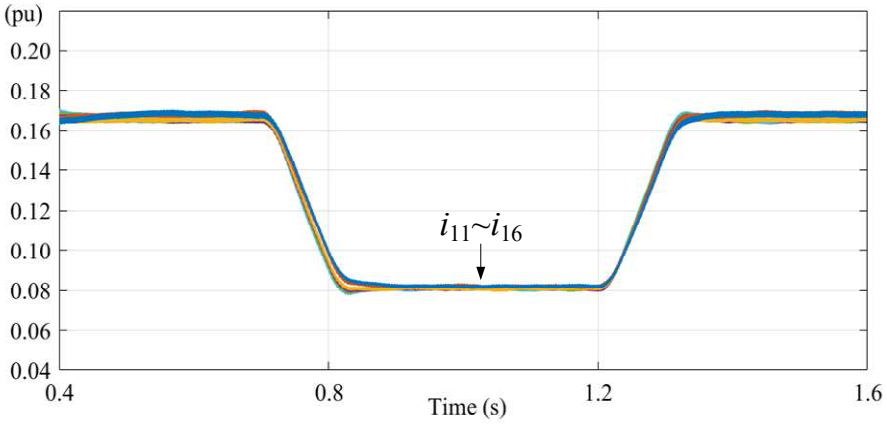

(c) Cell input average currents of Module 1

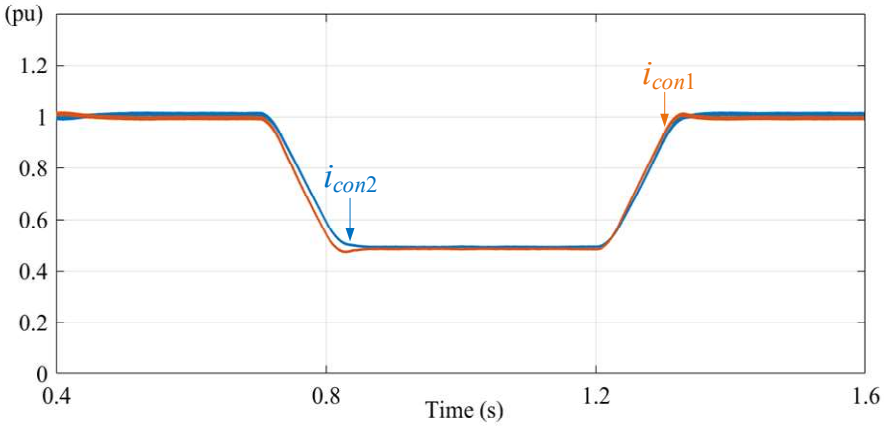

(d) Modular converter currents

Fig. 2-6 Stepped input wind speed simulations.

2.4 Summary

This chapter proposes a novel CSC-based MV ultra-high-power WECS, combining an MV six-phase generator with MFT-based modular converters. Compared with the existing CSC-based WECS with the passive rectifier, the proposed system effectively mitigates the rotor torque ripple, thereby extending the generator's lifespan and enhancing its efficiency. Meanwhile, a case study is provided to design the converters on the generator side.

Additionally, the modular converter has voltage and current imbalance issues, which are analyzed in detail. Based on the results of the analysis, a corresponding control scheme that implements input capacitor voltage balance control, cell current balance control, and converter current control is proposed. Simulation results verify the feasibility of the proposed WECS.

Chapter 3 An Online Selective Harmonic Elimination for Dual-Bridge Current Source Inverters in Wind Energy Conversion System

The grid-side converters of the proposed WECS adopt the dual-bridge CSIs utilizing the conventional SHE modulation. The SHE achieves superior harmonics with a minimum switching frequency and is well-used for dual-bridge CSIs. However, it is an offline modulation, resulting in large usage of digital controller memory in the case of the demand for the adjustable amplitude modulation index and the large look-up table.

This chapter introduces an online SHE modulation scheme for dual-bridge CSIs to address these issues, significantly reducing memory usage. Additionally, it retains all the benefits of conventional SHE. The feasibility of the online SHE is validated through simulation results.

3.1 Conventional SHE-Based Dual-Bridge CSIs

For the grid side of WECS, the primary control objectives for inverters are DC-link current control and reactive power control. Therefore, the dual-bridge CSIs have two modulation objectives: the adjustable amplitude modulation index (m_a) and delay angle (α) and eliminating the 11th and 13th harmonics of the PWM current. To meet the switching constraints of CSI, the modulation scheme includes Mode A and Mode B, which respectively suit (0, 0.85) and (0.85, 1) of amplitude modulation index (m_a). Considering that the proposed WECS operates in a high amplitude modulation index range (0.7, 1) for high efficiency, the operation ranges of Mode A and Mode B are (0.7, 0.84) and (0.84, 1), respectively.

The S_1 switching signal and the PWM current (i_{w1}) waveforms of Mode A are shown in Fig. 3-1. There are six pulses in the switching signal waveform, which means a 360 Hz switching frequency (fundamental frequency 60 Hz). In the PWM current waveform

i_{w1}, it has six pulses in the half-cycle with six switching angles in the first π/2 period where there are θ_1, θ_2, θ_3 and θ_4 as independent switching angles. All switching angles can be calculated based on these independent switching angles.

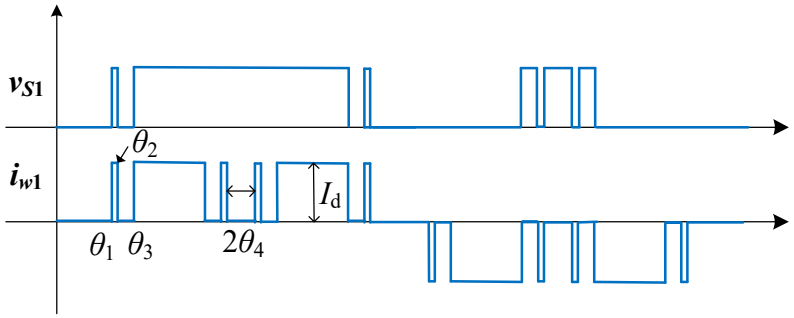

Fig. 3-1 Switching signal S_1 and PWM current i_{w1} waveforms of Mode A.

The waveforms of Mode B are depicted in the Fig. 3-2. There are seven pulses in the switching angle waveform, so the switching frequency is 420 Hz, and there are three independent switching angles in the PWM current waveform.

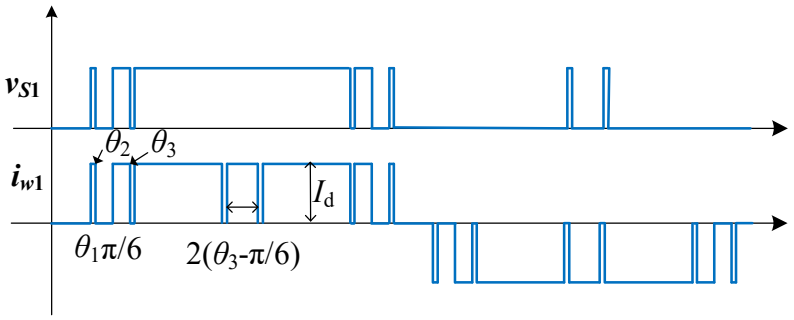

Fig. 3-2 Switching signal S_1 and PWM current i_{w1} waveforms of Mode B.

To eliminate the 11th and 13th harmonics of the PWM current and adjust m_a, the switching angles must have at least three degrees of freedom. Thus, Mode A and Mode B can achieve the modulation objectives.

As i_{w1} is a periodic waveform, it can be decomposed by Fourier into the following

formula:

$$i_{w1}(\omega t) = \sum_{n=1}^{\infty} a_n \sin(n\omega t), \tag{3-1}$$

where the Fourier coefficient can be expressed:

$$a_n = \frac{4}{\pi}\int_0^{\frac{\pi}{2}} i_{w1}(\omega t)\sin(n\omega t)d(\omega t). \tag{3-2}$$

For Mode A, it can be expanded as:

$$\begin{aligned} a_n &= \frac{4I_{dc}}{\pi}\left(\int_{\theta_1}^{\theta_2}\sin(n\omega t)d(\omega t) + \int_{\theta_3}^{\frac{\pi}{2}-\theta_4+\theta_1-\theta_3}\sin(n\omega t)d(\omega t) + \int_{\frac{\pi}{2}-\theta_4}^{\frac{\pi}{2}-\theta_4+\theta_1-\theta_2}\sin(n\omega t)d(\omega t)\right) \\ &= \cos(n\theta_1) - \cos(n\theta_2) + \cos(n\theta_3) - \cos\left(n\left(\frac{\pi}{2} - \theta_4 + \theta_1 - \theta_3\right)\right)... \\ &...+ \cos\left(n\left(\frac{\pi}{2} - \theta_4\right)\right) - \cos\left(n\left(\frac{\pi}{2} - \theta_4 + \theta_1 - \theta_2\right)\right) \end{aligned} \tag{3-3}$$

For Mode B, it can be expanded as:

$$\begin{aligned} a_n &= \frac{4I_{dc}}{\pi}\left(\int_{\theta_1}^{\theta_2}\sin(n\omega t)d(\omega t) + \int_{\frac{\pi}{6}}^{\theta_3}\sin(n\omega t)d(\omega t) + \int_{\frac{\pi}{3}-\theta_1}^{\frac{\pi}{3}+\theta_2}\sin(n\omega t)d(\omega t)...\right. \\ &...+ \left.\int_{\frac{2\pi}{3}-\theta_3}^{\frac{\pi}{2}}\sin(n\omega t)d(\omega t)\right) \\ &= \cos(n\theta_1) - \cos(n\theta_2) + \cos\left(n\frac{\pi}{6}\right) - \cos(n\theta_3) + \cos\left(n\left(\frac{\pi}{3} - \theta_1\right)\right) - \cos\left(n\left(\frac{\pi}{3} + \theta_2\right)\right)... \\ &...+ \cos\left(n\left(\frac{2\pi}{3} - \theta_3\right)\right) - \cos\left(n\frac{\pi}{2}\right) \end{aligned} \tag{3-4}$$

To eliminate the *i*th harmonic in i_{w1}, the *i*th equation can be formulated by setting a_i=0,

$$F_i = (\theta_1, \theta_2, ..., \theta_k) = 0, i = 1, 2, ..., k. \tag{3-5}$$

The fundamental waveform Fourier coefficient a_1 is set as m_a*I_{dc} to realize the adjustable amplitude modulation index m_a.

$$F_1 = (\theta_1, \theta_2, ..., \theta_k) = m_a, i = 1, 2, ..., k. \tag{3-6}$$

Therefore, to eliminate the 11th and 13th harmonics in i_{w1} and adjust m_a, Mode A and Mode B switching angles equations can be expressed:

$$ModeA:\begin{cases} F_1=\cos(\theta_1)-\cos(\theta_2)+\cos(\theta_3)-\cos(\frac{\pi}{2}-\theta_4+\theta_1-\theta_3)... \\ ...+\cos(\frac{\pi}{2}-\theta_4-\theta_2+\theta_1)-\cos(\frac{\pi}{2}-\theta_4)=m_a\frac{\pi}{4} \\ F_2=\cos(11\theta_1)-\cos(11\theta_2)+\cos(11\theta_3)-\cos(11(\frac{\pi}{2}-\theta_4+\theta_1-\theta_3))... \\ ...+\cos(11(\frac{\pi}{2}-\theta_4-\theta_2+\theta_1))-\cos(11(\frac{\pi}{2}-\theta_4))=0 \\ F_3=\cos(13\theta_1)-\cos(13\theta_2)+\cos(13\theta_3)-\cos(13(\frac{\pi}{2}-\theta_4+\theta_1-\theta_3))... \\ ...+\cos(13(\frac{\pi}{2}-\theta_4-\theta_2+\theta_1))-\cos(13(\frac{\pi}{2}-\theta_4))=0 \\ F_4=\theta_1-\frac{\pi}{6}-\theta_4=0 \end{cases} \quad (3\text{-}7)$$

$$ModeB:\begin{cases} F_1=\cos(\theta_1)-\cos(\theta_2)+\cos(\frac{\pi}{6})-\cos(\theta_3)+\cos(\frac{\pi}{3}-\theta_1)... \\ ...-\cos(\frac{\pi}{3}+\theta_2)+\cos(\frac{2\pi}{3}-\theta_3)-\cos(\frac{\pi}{2})=m_a\pi/4 \\ F_2=\cos(11\theta_1)-\cos(11\theta_2)+\cos(11(\frac{\pi}{6}))-\cos(11\theta_3)+\cos(11(\frac{\pi}{3}-\theta_1))... \\ ...-\cos(11(\frac{\pi}{3}+\theta_2))+\cos(11(\frac{2\pi}{3}-\theta_3))-\cos(11(\frac{\pi}{2}))=0 \\ F_3=\cos(13\theta_1)-\cos(13\theta_2)+\cos(13(\frac{\pi}{6}))-\cos(13\theta_3)+\cos(13(\frac{\pi}{3}-\theta_1))... \\ ...-\cos(13(\frac{\pi}{3}+\theta_2))+\cos(13(\frac{2\pi}{3}-\theta_3))-\cos(13(\frac{\pi}{2}))=0 \end{cases} \quad (3\text{-}8)$$

However, these equations are nonlinear and transcendental, making them difficult to solve directly. The Newton-Raphson iteration algorithm is an effective method to solve these equations [33]. The Newton-Raphson method is based on the Taylor expansion of the function and the approximation of the first derivative, which aims to find the root of the function by iteration. After an initial guess is given, it is iteratively updated. The flowchart of this algorithm is shown in Fig. 3-3, where θ^0 is the initial guess value of switching angles, and $\partial F/\partial\theta$ is the Jacob matrix given by:

$$ModeA:\frac{\partial F}{\partial\theta}=\begin{pmatrix} \frac{\partial F_1}{\partial\theta_1} & \frac{\partial F_1}{\partial\theta_2} & \frac{\partial F_1}{\partial\theta_3} & \frac{\partial F_1}{\partial\theta_4} \\ \frac{\partial F_2}{\partial\theta_1} & \frac{\partial F_2}{\partial\theta_2} & \frac{\partial F_2}{\partial\theta_3} & \frac{\partial F_2}{\partial\theta_4} \\ \frac{\partial F_3}{\partial\theta_1} & \frac{\partial F_3}{\partial\theta_2} & \frac{\partial F_3}{\partial\theta_3} & \frac{\partial F_3}{\partial\theta_4} \\ \frac{\partial F_4}{\partial\theta_1} & \frac{\partial F_4}{\partial\theta_2} & \frac{\partial F_4}{\partial\theta_3} & \frac{\partial F_4}{\partial\theta_4} \end{pmatrix}. \quad (3\text{-}9)$$

$$ModeB:\frac{\partial F}{\partial \theta}=\begin{pmatrix}\frac{\partial F_1}{\partial \theta_1} & \frac{\partial F_1}{\partial \theta_2} & \frac{\partial F_1}{\partial \theta_3}\\ \frac{\partial F_2}{\partial \theta_1} & \frac{\partial F_2}{\partial \theta_2} & \frac{\partial F_2}{\partial \theta_3}\\ \frac{\partial F_3}{\partial \theta_1} & \frac{\partial F_3}{\partial \theta_2} & \frac{\partial F_3}{\partial \theta_3}\end{pmatrix}. \tag{3-10}$$

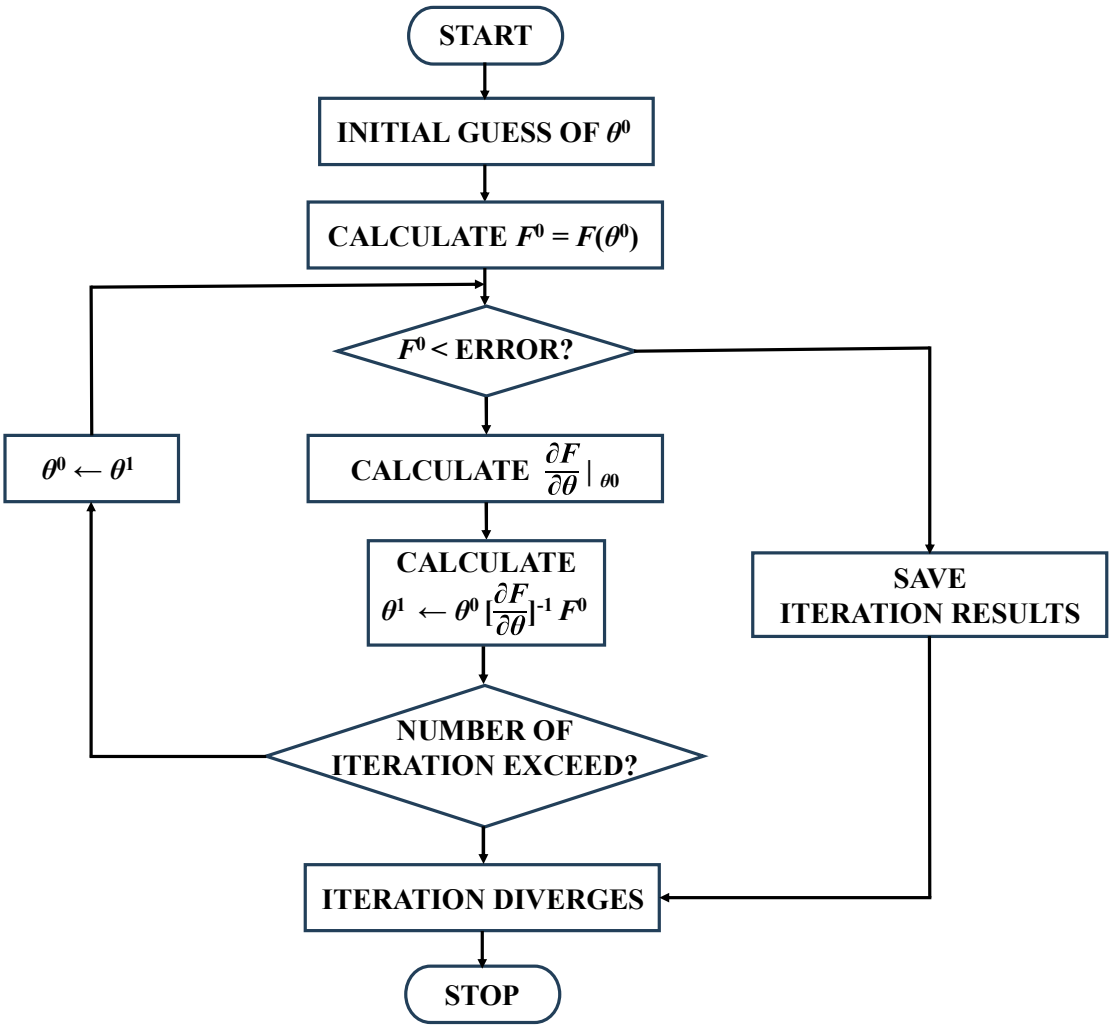

Fig. 3-3 Newton-Raphson iteration algorithm flowchart.

According to the equations (3-7) and (3-8), the Newton-Raphson iteration algorithm can obtain the switching angles. The number of data points for each switching angle directly determines the accuracy of the look-up table, but a larger look-up table can lead to a longer look-up time and larger memory usage. Considering the balance between accuracy and look-up time, the number of data points for each switching angle is set as

1000*1.035 from m_a=0.05 to m_a=1.085, which means the accuracy of m_a is 0.001. Then, they can form the look-up table and then be stored in the memory of the digital controller.

Fig. 3-4 shows the switching signals (S_1, S_2, …, S_6) and the PWM current i_{w1}, where the switch signals $S_1 \sim S_6$ have a phase difference of 60° between each successive signal. Meanwhile, the switch signals $S_7 \sim S_{12}$ of CSI 2 have a 30° difference from the switch signals $S_1 \sim S_6$, respectively.

The elimination of the 5th, 7th, 17th, and 19th harmonics in output current is achieved using a phase-shifting transformer connected to the outputs of the CSIs. The phase-shifting transformer consists of a wye-connected three-phase winding, a delta-connected three-phase winding on the primary side, and a wye-connected three-phase winding on the secondary side. This configuration provides phase shifts of 0° and 30° for the PWM currents of CSI 1 and CSI 2, respectively, which is combined with a 30° phase difference of switching signals between CSI 1 and CSI 2, leading to eliminating the 5th, 7th, 17th, and 19th harmonics of the output currents.

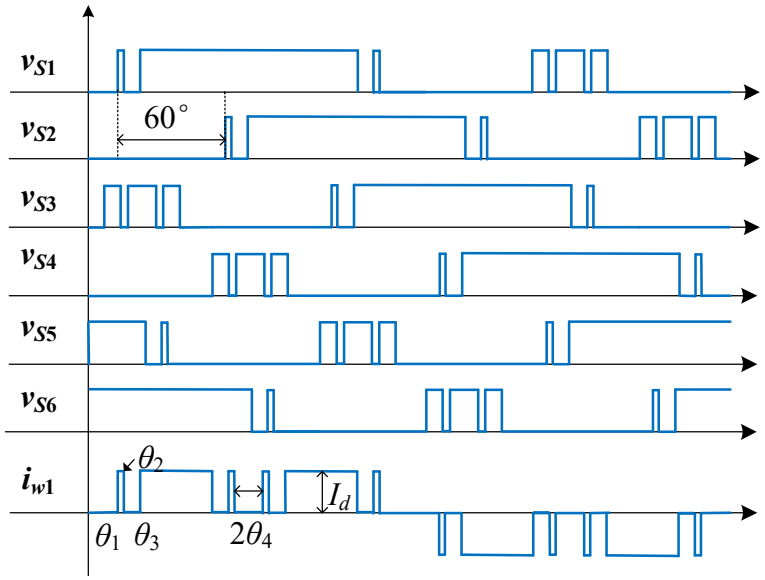

(a) Mode A

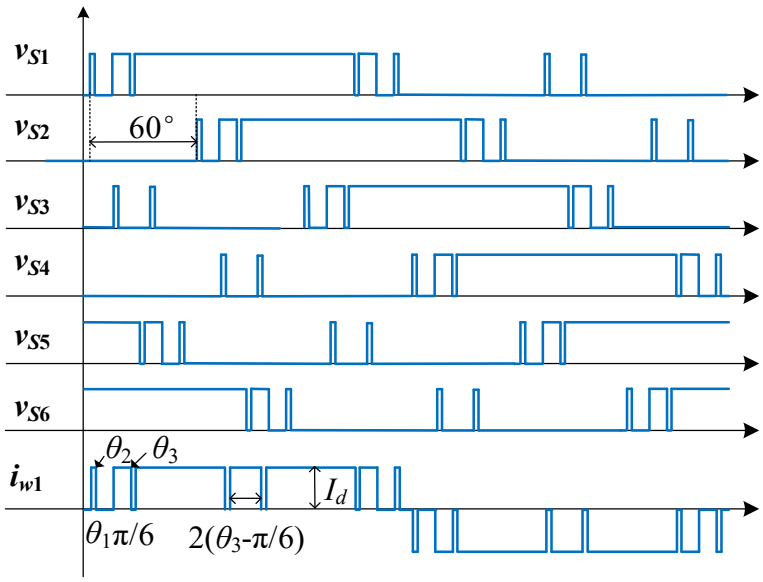

(b) Mode B

Fig. 3-4 SHE pulse-width modulation.

The configuration of the phase-shifting transformer is shown in Fig. 3-5, where the current phase of i_{A1} is set as 0°. For the primary wye-connected windings, the secondary equivalent currents retain the same phase as the primary currents, as expressed:

$$i_{a1} = \frac{1}{2}(\hat{I}_1 \sin(\omega t) + \hat{I}_5 \sin(5\omega t) + \hat{I}_7 \sin(7\omega t) + \hat{I}_{17} \sin(17\omega t) + \hat{I}_{19} \sin(19\omega t) + ...) \cdot \quad (3\text{-}11)$$

For the primary delta-connected windings, the secondary equivalent currents exhibit a phase difference of 30° relative to the primary currents, as expressed:

$$\begin{aligned} i_{a2} &= \frac{1}{2}(\hat{I}_1 \sin(\omega t + 30^\circ - 30^\circ) + \hat{I}_5 \sin(5(\omega t + 30^\circ) + 30^\circ) + \hat{I}_7 \sin(7(\omega t + 30^\circ) - 30^\circ)... \\ &... + \hat{I}_{17} \sin(17(\omega t + 30^\circ) + 30^\circ) + \hat{I}_{19} \sin(19(\omega t + 30^\circ) - 30^\circ) + ...) \\ &= \frac{1}{2}(\hat{I}_1 \sin(\omega t) - \hat{I}_5 \sin(5\omega t) - \hat{I}_7 \sin(7\omega t) - \hat{I}_{11} \sin(11\omega t)... \\ &... - \hat{I}_{17} \sin(17\omega t) - \hat{I}_{19} \sin(19\omega t) + ...) \end{aligned} \quad , \quad (3\text{-}12)$$

where the 30° phase shift indicated in the harmonic order brackets originates from the switching signal phase shift between CSI 1 and CSI 2. Consequently, output currents into the national grid, namely the secondary currents of the transformer, do not contain harmonics lower than the 23rd.

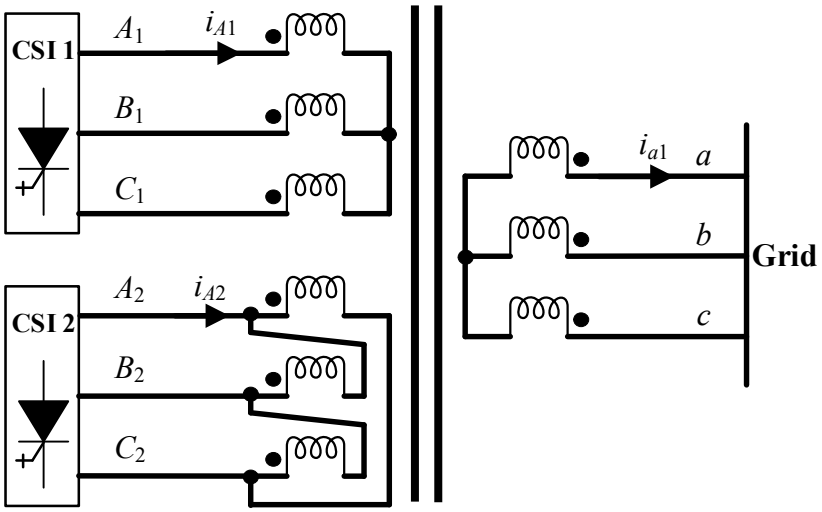

Fig. 3-5 Configuration of the phase-shifting transformer.

3.2 Online SHE-Based Dual-Bridge CSIs

The offline SHE modulation pre-calculates the switching angles to form the look-up table by switching angles equations and then stores the look-up table in the memory of the digital controller. However, to achieve high accuracy, this modulation scheme requires storing many discrete switching angles, leading to significant memory demands.

Unlike the offline SHE, the online SHE calculates switching angles in real-time by using continuous polynomial functions. Based on the look-up table, the discrete independent switching angles can be fitted into continuous polynomial functions by the fitting software, such as MATLAB's Polyfit function.

In the Polyfit function, the number of each switching angle in the look-up table must exceed the order of the polynomial function. Although a higher polynomial order provides greater accuracy, it requires longer computation time, which can degrade dynamic performance. Based on the look-up table obtained in Section 3.1, a trade-off of the polynomial orders is made between accuracy and time-consuming. As a result, the order of the polynomial function of Mode A and Mode B are set as 2 and 1, respectively. The resulting fitted continuous polynomial functions are expressed as:

$$
\begin{aligned}
ModeA:&\begin{cases}
\theta_{1F} = 100.659m_a^2 - 190.699m_a + 119.606 \\
\theta_{2F} = 147.452m_a^2 - 256.725m_a + 146.106 \\
\theta_{3F} = 44.148m_a^2 - 90.383m_a + 86.22 \\
\theta_{4F} = 100.659m_a^2 - 190.699m_a + 89.606
\end{cases}, \\
ModeB:&\begin{cases}
\theta_{1F} = 3.643m_a + 15.795 \\
\theta_{2F} = 15.17m_a + 5.922 \\
\theta_{3F} = 15.097m_a - 21.239
\end{cases}
\end{aligned}
\tag{3-13}
$$

Where θ_{1F}~θ_{4F} represent fitted values calculated by fitted polynomial functions, in these polynomial functions, the independent switching angles are the dependent variables, and m_a is the independent variable.

The trajectories of discrete switching angles and fitted polynomial functions are plotted in Fig. 3-6, where the polynomial functions closely approximate the discrete trajectories.

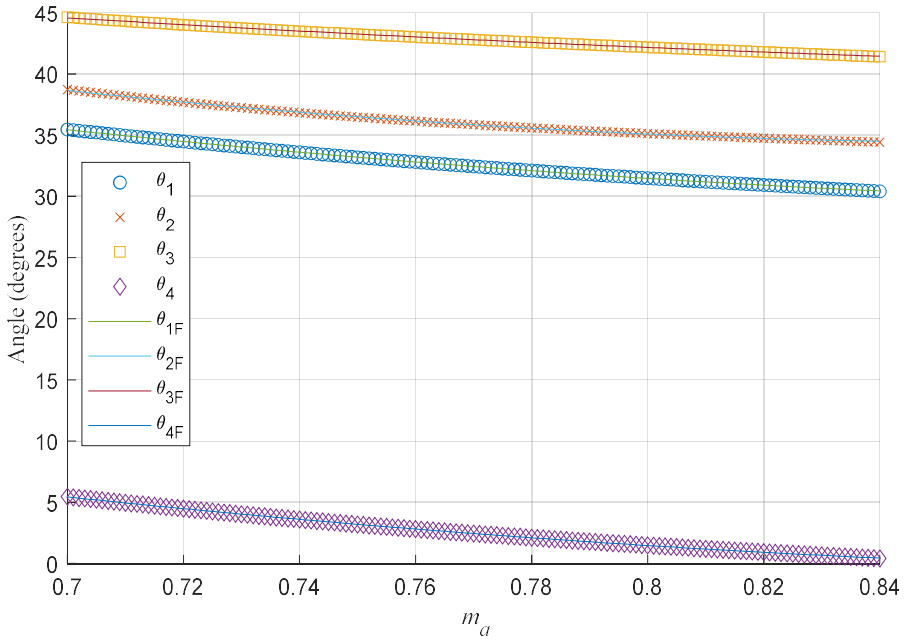

(a) Mode A

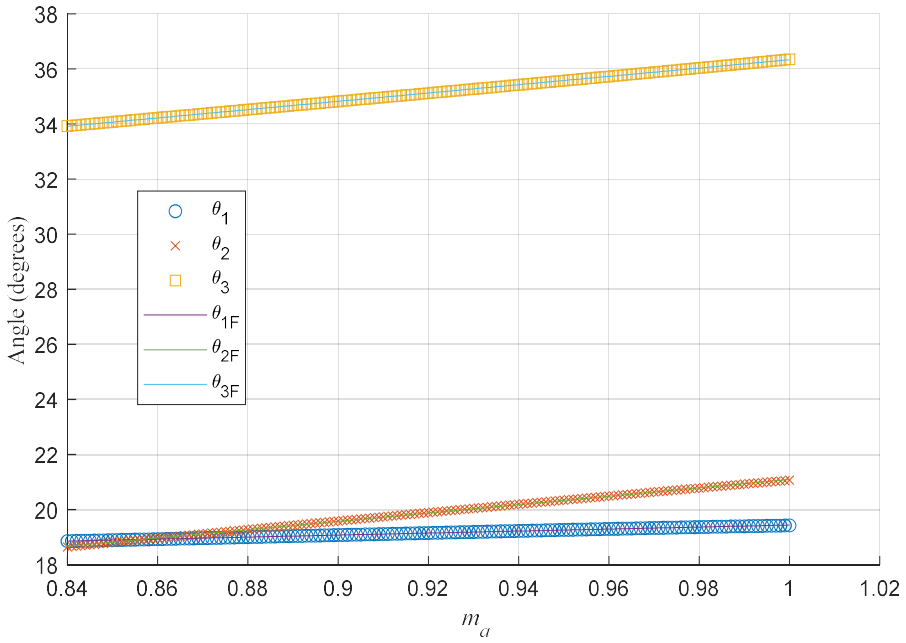

(b) Mode B

Fig. 3-6 Trajectories of discrete switching angles and polynomial functions.

To quantify the accuracy of the polynomial fitting, an absolute error index is defined:

$$\Delta\theta_i = |\theta_i - \theta_{iF}|, \tag{3-14}$$

The absolute errors between fitting and discrete real switching angles are plotted in Fig. 3-7, where the absolute errors of Mode A and Mode B are less than 0.08 and 0.02, respectively.

The above analysis shows that fitted polynomial functions of Mode B have lower order and higher accuracy than Mode A. For the CSIs of the proposed WECS, the high m_a can bring high DC utilization, leading to a smaller DC-link current at the same power, which means a smaller transmission loss. Therefore, the proposed control scheme makes the dual-bridge CSIs operate at high m_a. Especially when the DC-link current reference is determined by the grid side, CSIs operate at m_a=1. As a result, the CSIs of the proposed WECS mainly operate in Mode B, namely ma over 0.84. Therefore, the high accuracy and low order characteristic of Mode B is quite beneficial to the CSIs of the proposed WECS.

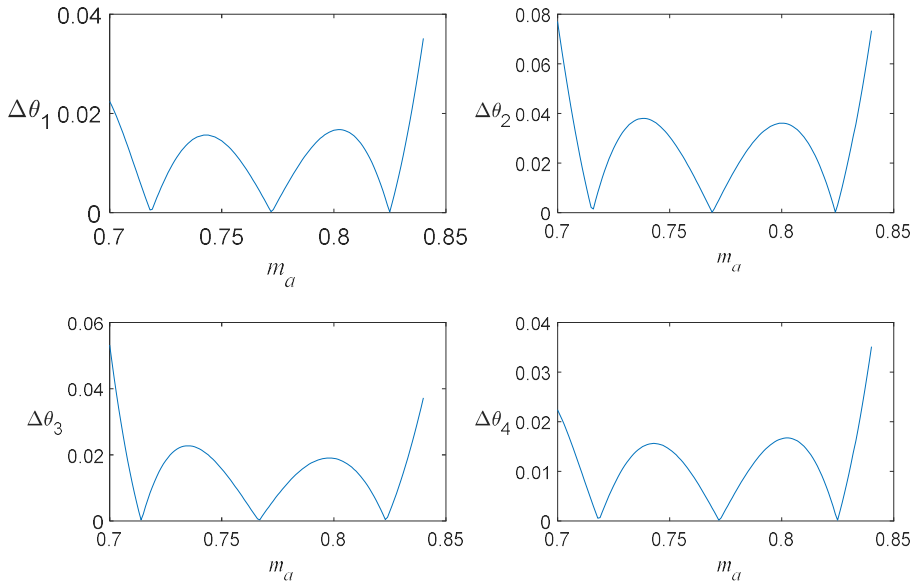

(a) Mode A

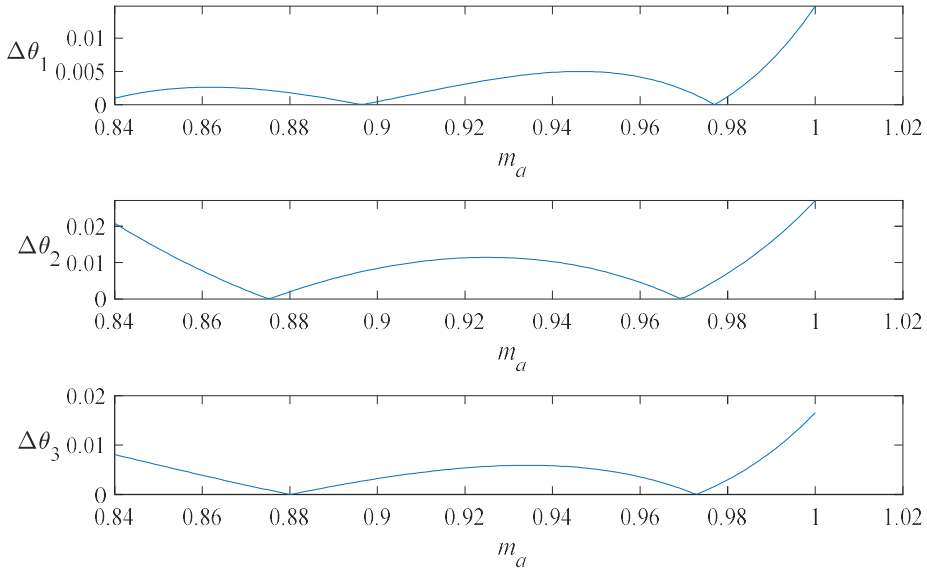

(b) Mode B

Fig. 3-7 Errors between fitting and discrete real switching angles.

A case study is provided to compare the online SHE with the conventional SHE. The DSP TMS320F28377S, developed by Texas Instruments, is a high-performance digital signal processor commonly used in industrial applications such as inverters, DC-DC

converters, and uninterruptible power supplies (UPS). The fast computation and robust PWM modules are ideal for power management and energy conversion tasks. In this case study, depending on the data type, all data in the look-up table and the polynomials are stored in the 32-bit floating-point form. The memory usage comparison between online SHE and offline SHE is shown in Table 3-1.

Table 3-1 Memory usage comparison between Online SHE and Offline SHE

Parameter	Online SHE (Fitted Polynomial Function)		Offline SHE (Look-up Table)	
Operation Mode	Mode A	Mode B	Mode A	Mode B
Memory Consumption	48 B	24 B	2.75 KB	2.52 KB

The table shows that the online SHE requires substantially less memory than the conventional approach. Consequently, it is evident that online SHE has smaller memory usage than offline SHE.

3.3 Simulation Results

The feasibility of the online SHE in dual-bridge CSIs is verified by the simulation results based on MATLAB/Simulink. The simulations are classified into three parts: (1) the principle of dual-bridge CSIs verification simulations, (2) the steady harmonic performance comparison simulations between offline SHE and online SHE and (3) the dynamic performance simulation in stepped input wind speed for online SHE.

The phase-shifting transformer adopts the three-winding linear transformer model in the Simulink library. The switch devices adopt the Gate turn-off thyristor (GTO) model. The simulation system parameters are based on Table 2-2. The parameters of dual-bridge CSIs are shown in Table 3-2, where the filter parameters are designed so that the THD meets the grid code for all m_a, namely, THD lower than 5%. The national grid uses a three-phase voltage source as a substitute.

Table 3-2 Dual-bridge CSI parameters

Parameter	Value	Parameter	Value
Number of Turns of the Primary Wye Connection	1000	Filter Inductance	100 μH
Number of Turns of the Primary Delta Connection	1732	Filter Capacitor	20 μF
Number of Turns of the Secondary Delta Connection	2000	DC-link Inductance	50 mH

As CSIs in this thesis mainly operate in the conditions of high m_a for high efficiency, Fig. 3-8 shows the final output current spectrum flowing into the grid, where the harmonics lower than 23rd are completely eliminated. The output current THD of m_a=1 (Mode A) is 3.38% lower than 4.22% of m_a=0.8 (Mode B). The simulation results prove the principal analysis of dual-bridge CSIs.

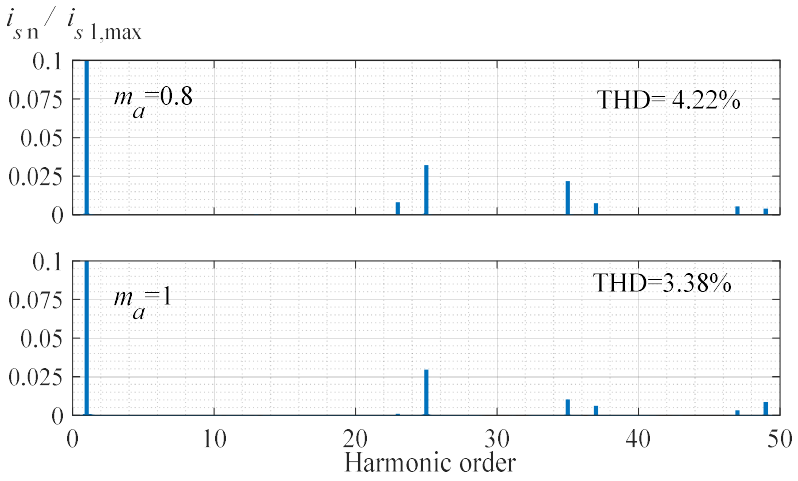

Fig. 3-8 Online SHE steady output current spectrum.

To evaluate the harmonic performance difference between online SHE and offline SHE, simulations are implemented from m_a=0.1 to m_a=1, and the step size is 0.1. For each simulation, the proportions of the harmonics to the maximum fundamental current

$i_{w1,\max}$ are recorded, where $i_{w1,\max}$ is equal to DC-link current I_{dc}. The harmonics in the PWM current are mainly low order, so the 5th, 7th, 17th and 19th harmonics are recorded. These statistics are plotted in Fig. 3-9, the harmonic content of the PWM current i_{w1} comparison between online SHE and offline SHE.

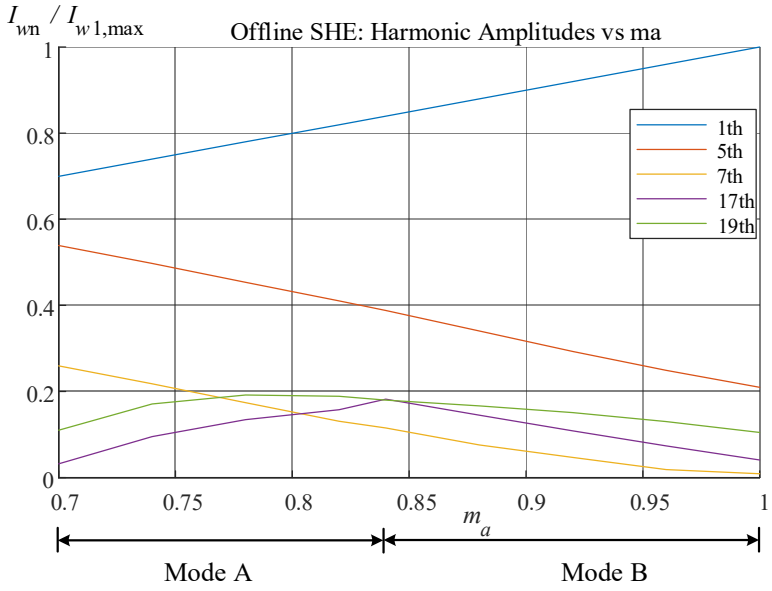

(a) Offline SHE

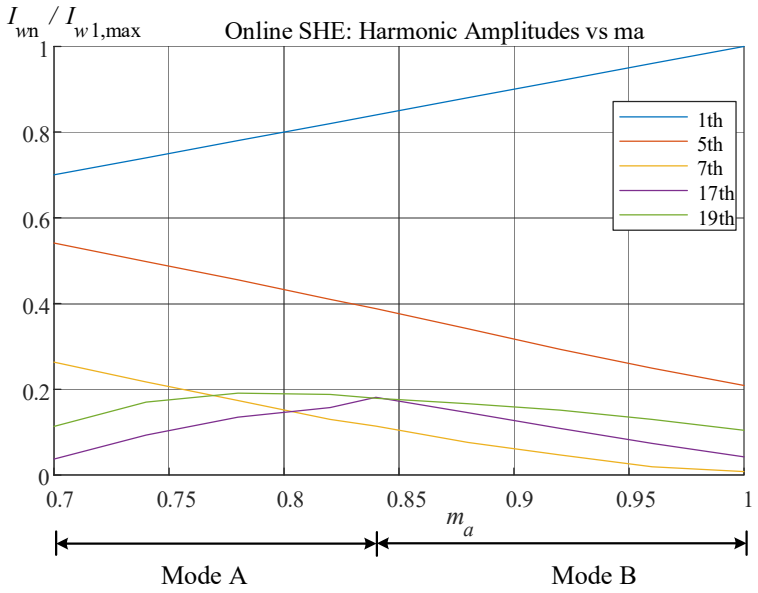

(b) Online SHE

Fig. 3-9 Harmonic content of PWM current i_{w1} comparison between online SHE and offline SHE.

From the figures, both waveforms are the same, which verifies that the online SHE has almost the same harmonic performance as the offline SHE. Therefore, online SHE retains the merit of good harmonic performance offline.

Figure 3-10 illustrates the simulation under stepped input wind speed conditions. The wind speed decreases from 12 m/s to 10 m/s between t = 0.7 s and 0.8 s and subsequently increases from 10 m/s to 12 m/s between t=1.2 s and t=1.3 s. The DC-link current reference dynamically adjusts according to the wind speed to achieve minimum current operation, reducing the loss of power, with the current closely tracking the reference variation, as shown in the figure. These results demonstrate that the online SHE method achieves good dynamic performance under varying wind speed conditions.

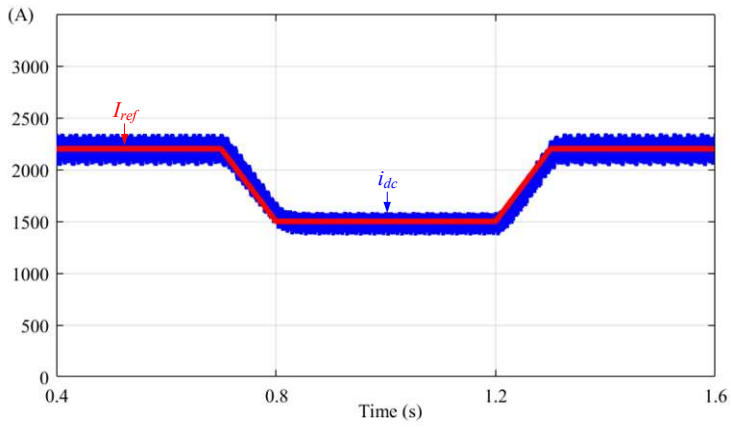

Fig. 3-10 Simulation in stepped input wind speed.

Figure 3-11 illustrates the simulation of reactive power control, where voltage and current unit base are the peak values of grid phase voltage 5882 V and current 801 A. The currents (i_{ga}) injected into the grid are controlled in the same phase with grid voltages VA by reactive power control, so the reactive power injected into the grid is zero, and the power factor is 1.

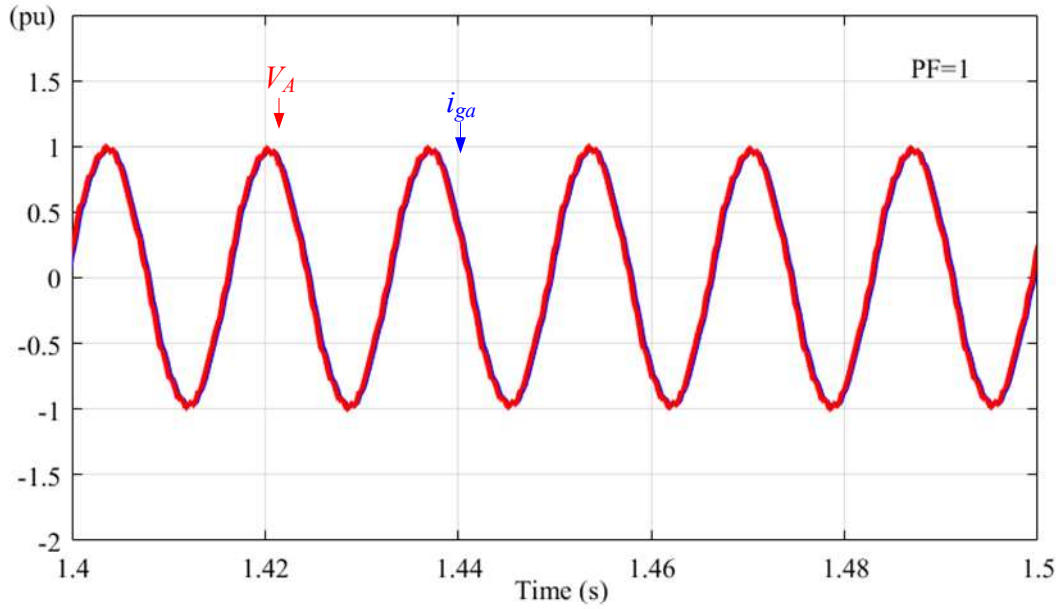

Fig. 3-11 Simulation of reactive power control.

Consequently, these simulations verify the principles of dual-bridge CSIs, demonstrate that online SHE achieves the same harmonic performance as offline SHE, and confirm the DC-link current control under stepped wind speed conditions and reactive power control.

3.4 Summary

This Chapter applies the online SHE to the dual-bridge CSIs. It allows switching angles to be calculated in real-time by fitted polynomial functions, significantly saving the memory of the digital controller. In addition, all the advantages of conventional SHE are retained. A case study is provided to quantitatively verify this conclusion. Finally, the feasibility of online SHE is validated through simulation.

Chapter 4 Conclusions

This thesis proposes a novel current source converter-based ultra-high-power offshore wind energy conversion system. The work mainly includes proposing a new configuration of WECS and a corresponding control scheme and applying an online SHE modulation scheme to the generator-side CSIs. This chapter summarizes the thesis's contributions and conclusions, along with an outline of potential directions for future work.

4.1 Contributions and Conclusions

The contributions and conclusions are summarized as follows:

(1) A novel CSC-based ultra-high-power offshore WECS is proposed.

The following discussion focuses on the existing offshore CSC-based WECS. Compared to the LFT-based WECS, the proposed system achieves a smaller size and weight, primarily due to the integration of MFT. When contrasted with MFT-based WECS utilizing an active rectifier, the proposed system offers several advantages, including reduced cost, enhanced efficiency, and improved reliability attributed to the utilization of a diode rectifier. Furthermore, compared to the MFT-based WECS equipped with a diode rectifier, the proposed system effectively mitigates rotor torque ripple and enhances reliability and efficiency by employing a six-phase generator.

(2) A corresponding control scheme is proposed.

The proposed WECS faces voltage and current imbalance issues due to its input series-parallel structure. The proposed control scheme effectively addresses the voltage and current imbalance issues.

(3) An online SHE modulation scheme is applied to the grid-side dual-bridge CSIs.

The online SHE modulation employs fitted polynomial functions to generate switching angles in real-time, significantly conserving the digital controller's memory

and thereby minimizing the demand for memory.

4.2 Future Work

Several potential directions will be suggested for research in the future, including improving overall efficiency and reducing costs and footprints.

(1) The modular converter will be further optimized to improve the output voltage gain so that the transmission current in the DC-link can be reduced, leading to higher overall efficiency.

(2) The multiple bridge CSIs combined with phase-shifting transformers are a good direction to further improve the harmonic performance, reducing the size and costs of output filters or lowering the switching losses.

References

[1] V. Yaramasu, B. Wu, and C. S. Paresh, "High-power wind energy conversion systems: State-of-the-art and emerging technologies," *Proceedings of the IEEE*, vol. 103, no. 5, pp. 740–788, 2015.

[2] B. Wu, *High-Power Converters and AC Drives*. New York, NY, USA: Wiley, 2006.

[3] M. Popat, B. Wu, and N. R. Zargari, "Fault ride-through capability of cascaded current-source converter-based offshore wind farm," *IEEE Transactions on Sustainable Energy*, vol. 4, no. 2, pp. 314–323, 2013.

[4] *PCS6000 Medium voltage wind turbine converter*, ABB Group, Zurich, Switzerland, 2023. [Online]. Available: https://new.abb.com/power-converters-inverters/wind-turbines/utility-scale/pcs6000.

[5] *Enewin Series*, YASKAWA Asean, Singapore, 2010. [Online]. Available: https://www.yaskawa.com.sg/product/large-wind-turbine/enewin-series.

[6] N. Holtsmark, H. J. Bahirat, M. Molinas, B. A. Mgork, and H. K. Høidalen, "An all-DC offshore wind farm with series-connected turbines: An alternative to the classical parallel AC model?" *IEEE Transactions on Industrial Electronics*, vol. 60, no. 6, pp. 2420–2428, 2013.

[7] A. Garcés and M. Molinas, "A study of efficiency in a reduced matrix converter for offshore wind farms," *IEEE Transactions on Industrial Electronics*, vol. 59, no. 1, pp. 184–193, 2012.

[8] A. B. Mogstad, M. Molinas, P. K. Olsen and R. Nilsen, "A power conversion system for offshore wind parks," *2008 34th Annual Conference of IEEE Industrial Electronics*, Orlando, FL, USA, 2008, pp. 2106-2112.

[9] Y. Xia, K. H. Ahmed, and B. W. Williams, "A PWM current source based DC transmission system for multiple wind turbine interfacing," *IEEE Journal of Emerging and Selected Topics in Power Electronics*, vol. 2, no. 4, pp. 784–796, 2014.

[10] Q. Wei, B. Wu, D. Xu, and N. R. Zargari, “A medium-frequency transformer-based wind energy conversion system used for the current-source converter-based offshore wind farm,” *IEEE Transactions on Power Electronics*, vol. 32, no. 1, pp. 248–259, 2017.

[11] Z. Wang and Q. Wei, “A New Current Source Converter-based Topology for Wind Energy Conversion Systems,” *2023 IEEE 14th International Symposium on Power Electronics for Distributed Generation Systems (PEDG)*, Shanghai, China, 2023, pp. 295-29.

[12] C. Meyer, M. Hoing, A. Peterson, and R. W. De Doncker, “Control and design of DC grids for offshore wind farms,” *IEEE Transactions on Industry Applications*, vol. 43, no. 6, pp. 1475–1482, 2007.

[13] S. Lundberg, “Configuration study of large wind parks,” Thesis, Masters in Electrical Engineering, Chalmers University of Technology, 2003.

[14] E. Veilleux and P. W. Lehn, “Interconnection of direct-drive wind turbines using a series-connected DC grid,” *IEEE Transactions on Sustainable Energy*, vol. 5, no. 1, pp. 139–147, 2014.

[15] M. J. Durán, S. Kouro, B. Wu, E. Levi, F. Barrero and S. Alepuz, “Six-phase PMSG wind energy conversion system based on medium-voltage multilevel converter,” *Proceedings of the 2011 14th European Conference on Power Electronics and Applications*, Birmingham, UK, 2011, pp. 1-10.

[16] J. Dai, D. Xu, and B. Wu, ‘‘A novel control scheme for current-source-converter-based PMSG wind energy conversion systems,’’ *IEEE Transactions on Power Electronics*, vol. 24, no. 4, pp. 963–972, 2009.

[17] L. Xing, Q. Wei and Y. Li, “A PWM Current-Source Converter-Based Wind Energy Conversion System,” *IEEE Transactions on Power Electronics*, vol. 39, no. 2, pp. 2787-2797, 2024.

[18] B. Wu, Y. Lang, N. Zargari, and S. Kouro, *Power Conversion and Control of Wind Energy Systems*. Hoboken, NJ, USA: Wiley, 2011.

[19] J. Dai, Y. Lang, B. Wu, D. Xu and N. Zargari, “A Multi-sampling SVM Scheme for Current Source Converter with Superior Harmonic Performance,” *2009 Twenty-Fourth Annual IEEE Applied Power Electronics Conference and Exposition*, Washington, DC, USA, 2009, pp. 132-138.

[20] Q. Wei, B. Wu, D. D. Xu, and N. R. Zargari, “Optimal space vector sequence investigation based on natural sampling SVM for medium voltage current-source converter,” *IEEE Transactions on Power Electronics*, vol. 32, no. 1, pp. 176–185, 2017.

[21] M. Popat, B. Wu, F. Liu, and N. R. Zargari, “Coordinated control of cascaded current-source converter based offshore wind farm,” *IEEE Transactions on Sustainable Energy*, vol. 3, no. 3, pp. 557–565, 2012.

[22] M. Popat, B. Wu, and N. R. Zargari, “A novel decoupled interconnecting method for current-source converter-based offshore wind farms,” *IEEE Transactions on Power Electronics*, vol. 27, no. 10, pp. 4224–4233, 2012.

[23] B. Wu, J. Pontt, J. Rodriguez, S. Bernet, and S. Kouro, “Current-Source Converter and Cycloconverter Topologies for Industrial Medium-Voltage Drives,” *IEEE Transactions on Industrial Electronics*, vol. 55, no. 7, pp. 2786–2797, 2008.

[24] Q. Wei, L. Xing, D. Xu, B. Wu, and N. R. Zargari, “Modulation Schemes for Medium Voltage PWM Current Source Converter-Based Drives: An Overview,” *IEEE Journal of Emerging and Selected Topics in Power Electronics*, vol. 7, no. 2, pp. 1152–1161, 2019.

[25] H. R. Karshenas, H. A. Kojori, S. B. Dewan and J. H. Choi, “Generalized techniques of selective harmonic elimination and current control in current source inverters/converters,” *Proceedings of 1994 IEEE Applied Power Electronics Conference and Exposition - ASPEC'94*, Orlando, FL, USA, 1994, pp. 107-114.

[26] K. Yang, M. Feng, Y. Wang, X. Lan, J. Wang, D. Zhu, and W. Yu, “Real-Time Switching Angle Computation for Selective Harmonic Control,” *IEEE Transactions on Power Electronics*, vol. 34, no. 8, pp. 8201–8212, 2019.

[27] M. Steczek, P. Chudzik, and A. Szelag, “Combination of SHE- and SHM-PWM Techniques for VSI DC-Link Current Harmonics Control in Railway Applications,” *IEEE Transactions on Industrial Electronics*, vol. 64, no. 10, pp. 7666–7678, 2017.

[28] M. Wu, L. Ding, C. Xue, and Y. W. Li, “Model-Based Closed-Loop Control for High-Power Current Source Rectifiers Under Selective Harmonic Elimination/Compensation PWM With Fast Dynamics,” *IEEE Journal of Emerging and Selected Topics in Power Electronics*, vol. 10, no. 5, pp. 5921–5932, 2022.

[29] Q. Wei, B. Wu, D. D. Xu, and N. R. Zargari, “Power balancing investigation of grid-side series-connected current source inverters in wind energy conversion systems,” *IEEE Transactions on Industrial Electronics*, to be published.

[30] Q. Wei, B. Wu, D. D. Xu, and N. R. Zargari, “An optimized strategy for PWM current source converter-based wind conversion system with reduced cost and improved efficiency,” *IEEE Transactions on Power Electronics*, to be published.

[31] Z. Chen, “Compensation schemes for a SCR converter in variable speed wind power systems,” *IEEE Transactions on Power Delivery*, vol. 19, no. 2, pp. 813–821, 2004.

[32] IEEE C57.12.00-2020, p. 64, 9.2.

[33] B. Wu, “Pulse Width Modulated Current Source Inverter (CSI) Induction Motor Drives,” Thesis, Masters in Applied Science, University of Toronto, 1989.